The Astrophysical Journal, 851:44 (21pp), 2017 December 10 https://doi.org/10.3847/1538-4357/aa99d5

Cosmic Star Formation: A Simple Model of the SFRD(z)

Cesare Chiosi[1,2], Mauro Sciarratta[1], Mauro D'Onofrio[1,2], Emanuela Chiosi[2], Francesca Brotto[1], Rosaria De Michele[1], and Valeria Politino[1]
[1] Department of Physics and Astronomy, University of Padova, Vicolo Osservatorio 3, I-35122 Padova, Italy; cesare.chiosi@unipd.it
[2] INAF Observatory of Padova, Vicolo Osservatorio 5, I-35122 Padova, Italy
Received 2017 June 7; revised 2017 October 17; accepted 2017 November 6; published 2017 December 11

Abstract

We investigate the evolution of the cosmic star formation rate density (SFRD) from redshift $z = 20$ to $z = 0$ and compare it with the observational one by Madau and Dickinson derived from recent compilations of ultraviolet (UV) and infrared (IR) data. The theoretical SFRD(z) and its evolution are obtained using a simple model that folds together the star formation histories of prototype galaxies that are designed to represent real objects of different morphological type along the Hubble sequence and the hierarchical growing of structures under the action of gravity from small perturbations to large-scale objects in Λ-CDM cosmogony, i.e., the number density of dark matter halos $N(M, z)$. Although the overall model is very simple and easy to set up, it provides results that mimic results obtained from highly complex large-scale *N*-body simulations well. The simplicity of our approach allows us to test different assumptions for the star formation law in galaxies, the effects of energy feedback from stars to interstellar gas, the efficiency of galactic winds, and also the effect of $N(M, z)$. The result of our analysis is that in the framework of the hierarchical assembly of galaxies, the so-called time-delayed star formation under plain assumptions mainly for the energy feedback and galactic winds can reproduce the observational SFRD(z).

Key words: dark matter – galaxies: evolution – galaxies: luminosity function, mass function – galaxies: photometry – galaxies: star formation – large-scale structure of universe

1. Introduction

This paper examines the problem of the global history of star formation and chemical enrichment of the whole Universe, otherwise known as the baryon budget in galactic halos or as the history of the so-called star formation rate density SFRD(z). Since the seminal studies by Tinsley (1980) and Madau et al. (1996), cosmic star formation has been the subject of numberless papers that are impossible to recall here. The evolution of the SFRD(z) over cosmic times is crucial for understanding galaxy formation and evolution and for constraining any theory devoted to this subject (Hopkins 2004; Wilkins et al. 2008; Guo et al. 2011; Bouwens et al. 2012; Cucciati et al. 2012; Tescari et al. 2014; Abramson et al. 2016; Katsianis et al. 2017). The evolution of the SFRD(z) is known today with unprecedented accuracy up to the distant Universe, thanks to the multi-wavelength surveys carried out by many groups, among which we recall Bernardi et al. (2010), González et al. (2011), Bouwens et al. (2012), Lee et al. (2011), Smit et al. (2012), Santini et al. (2012), Schenker et al. (2013), van der Burg et al. (2010), Gruppioni et al. (2013), Parsa et al. (2016), Reddy et al. (2008), Magnelli et al. (2011), Sobral et al. (2013), Alavi et al. (2014), Cucciati et al. (2012), and Ly et al. (2011). The situation has recently been systematically summarized and reviewed by Madau & Dickinson (2014) and Katsianis et al. (2017), to whom we refer for all details.

The interpretation of the cosmic SFRD(z) has been addressed by many theoretical studies, among which we recall Rasera & Teyssier (2006), Hernquist & Springel (2003), and Katsianis et al. (2017), with either analytical or semi-analytical or hydrodynamical simulations. In particular, they investigated the effect of the energy feedback from supernovae explosions, stellar winds, and active galactic nuclei (AGN) activity on modeling the cosmic star formation. They made use of an improved version of the P-GADGET3 of Springel (2005) with chemical enrichment (Tornatore et al. 2007), supernova energy and momentum-driven galactic winds (Puchwein & Springel 2013), AGN feedback (Springel et al. 2005a; Planelles et al. 2013), metal-line cooling (Wiersma et al. 2009b, 2009a) plus molecules/metal cooling (Maio et al. 2007), supernova-driven galactic winds with feedback (Barai et al. 2013), thermal conduction (Dolag et al. 2004), and other more technical details (see Tescari et al. 2014, for a more exhaustive description). In general, the shape of the SFRD(z) as a function of the redshift is reproduced by the models. However, according to Tescari et al. (2014), the SFRD(z) is insensitive to feedback at $z > 5$, unlike to what happens at lower redshifts. They find that the key factor for reproducing the observational SFRD is a combination of strong supernova-driven wind and early AGN feedback in low-mass galaxies. Similar conclusions are reached by Katsianis et al. (2017) in the sense that the AGN feedback they adopted decreases the SFRD at $z < 3$, but not sufficiently at higher redshift. According to the authors, the type of feedback one would need to reconcile observations and theory is a strong feedback at high redshifts and a less efficient one at low redshift. Katsianis and collaborators also show that variable galactic winds, which are efficient at decreasing the star formation rate (SFR) of low-mass galaxies, are quite successful in reproducing the observational data.

Although the theoretical SFRD(z) obtained in these studies nicely reproduces the observational one (which is expected since some important physical ingredients, such as the energy feedback from AGNs via the galactic winds on a galaxy SFR, have yielded the sought variation in cosmic SFRD with redshift), the results are not yet conclusive as far as the key physical process in shaping the cosmic SFRD(z) is concerned, however. Casting the question in a different way, we would like to understand whether the cosmic SFRD(z) is driven more by causes of external or internal nature.

Among the external causes, the dominant cause is the gravitational building-up of structures (the proto-galaxies made of dark and baryonic matter) via hierarchical aggregation, which leads to a mass function of galaxies that is not the same at different redshifts. Numerical simulations of cosmic mass aggregation show that the halo mass distribution function, i.e., the relative number of galaxies per mass interval, on one hand steepens with mass at increasing redshift, but even more importantly, several different solution are found (Murray et al. 2013, and references therein) that all merit exploration.

Among the internal causes, star formation is dominant: how it varies with the total mass and the mean density of the galaxy, how the SFR varies with time within a galaxy, and the physical properties of the interstellar medium. Another important issue is whether the SFR in a galaxy always starts at maximum efficiency and declines with time so that some "quenching mechanisms" must be invoked at very early epochs to explain the decline of the SFRD(z) at increasing redshift, or if it instead starts low, grows to a maximum, and then declines (typical of spheroidal systems), or alternatively remains mild and nearly constant (such as in disk-like objects). In some cases, it experiences a series of episodes (the so-called bursting model, typical of low-mass galaxies).

Finally, we would like to quantify the relative weight of the hierarchical aggregation compared to the intrinsic SFR. Most likely, both contribute to modeling the SFRD(z), but to which extent? Investigations based on large-scale numerical simulations that are possible with P-GADGET3-like codes have the gravitational aggregation built in by default so that only the effect of different prescriptions for the star formation and associated energy injection and feedback can be tested. On the other hand, testing the effects of the various physical ingredients with direct hydrodynamical large-scale simulations is expensive and time consuming. For these reasons, it is still useful and interesting to address the problem in a simple fashion by means of a semi-analytical model that is able to catch the essence of the problem.

The plan of the paper is as follows. In Section 2 we shortly review the present-day observational picture of the SFRD(z), recalling the main ways of measuring it, the various points of uncertainty, in particular the role of the stellar initial mass function (IMF), the variation of the star formation histories in galaxies of different type, and the distance determinations. In Section 3 we present the strategy of the present study, which is aimed at deriving the SFRD(z) from three elementary building blocks: (i) the current hierarchical view of galaxy formation, providing the expected number of galaxies (consisting of dark and baryonic matter) per unit volume (usually a Mpc^3) presented in Section 4; (ii) simple models of galaxy formation and evolution for different values of total mass and morphological type that are presented in Section 5 (they provide the rate of star formation, mass in stars, gas content, metallicity, and other useful properties of individual galaxies); and (iii) finally, the evolutionary population synthesis technique that is used to derive the magnitudes and colors of the model galaxies as function of time (redshift), which is presented in Section 6. In Section 7 we combine the results of the previous sections, derive the cosmic SFRD, and compare it to observational data. In order to highlight and single out the role played by the galaxy number density distribution and the galaxy SFR at different epochs, we perform some ad hoc simulations by varying some key assumptions and illustrate the results. Finally, in Section 8 some conclusive remarks are made.

2. The Cosmic Star Formation Rate

The SFRD(z) we intend to investigate and reproduce is the one presented by Madau & Dickinson (2014, and references therein). In general, to infer the SFRD(z) from the fluxes measured in suitable passbands (typically ultraviolet, UV, and near- and far-infrared, NIR and FIR, respectively) and to express it in masses per unit time and unit volume of space, one needs some assumptions about the correlation between the measured fluxes and the SFR, the corrections for the effect of dust on the absorbing part of the UV to reemit it in the NIR and FIR, the IMF together with some hints about its constancy or variation with time and space, the type of star formation at work on cosmic scales and Hubble time, and other details.

Several problems affect the determination of the SFRD(z), among which we briefly recall the following below.

Stellar mass census. Deriving the mass in stars (i.e., the underlying IMF) from their light is a cumbersome affair because it requires information on the mass-to-light ratio (*M/L*) of the stellar populations, which in turn depends on the age, the history of star formation, and the amount of dust around the star (extinction). In general, the conversion from light to mass is made through population synthesis models, which provide the relationship between mass in stars (both luminous and faint—hence invisible), the light emitted by them, and the relative number of stars born in different generations, all contributing to the light and the mass at present day; in other words, the history of star formation. Among other parameters, these models depend on the IMF. On the other hand, the IMF is difficult to determine directly from the observational data for several reasons that do not need to be examined here (see Madau & Dickinson 2014, for a detailed discussion of the issue). The obvious way out is to assume a certain IMF. The most popular IMF is the Salpeter (1955) law, even though it is known to predict *M/L* ratios higher than observed, thus requiring deep revision of the IMF at the low-mass end (see Kroupa et al. 1993; Hennebelle & Chabrier 2011; Chabrier 2015). Another difficulty affecting the stellar mass census is due to the detection of low-mass dusty galaxies. This means that a great portion of the stellar mass could be missing in current data.

Variations of the star formation history in galaxies. The star formation history (SFH) of a galaxy may greatly change over the years on both short and long timescales. Young stars indeed outshine old stars, thus affecting the total spectral energy distribution, and hence the total mass of the old stars may be largely underestimated, and the effect of old stars can hardly be singled out.

Distances. Finally, the sources of observational data change with distance, so that homogeneous data sets extending from the local pool all the way up to redshift $z \leqslant 10$ are not possible. For instance, in the local Universe ($0 < z < 1$), most of the IR data are not due to dust in star-forming regions, but to dust in the ISM. This trend tends to decrease with distance. In the redshift interval $1 < z < 4$, no IR data are measured for individual sources but for the hyper-luminous ones, which strongly affects the evaluation of the IR luminosity density. At higher redshifts, essentially only data for hyper-luminous sources are available, which exacerbates the problem. For all these reasons, Madau & Dickinson (2014) limit their analysis to the redshift interval $0 < z < 8$.

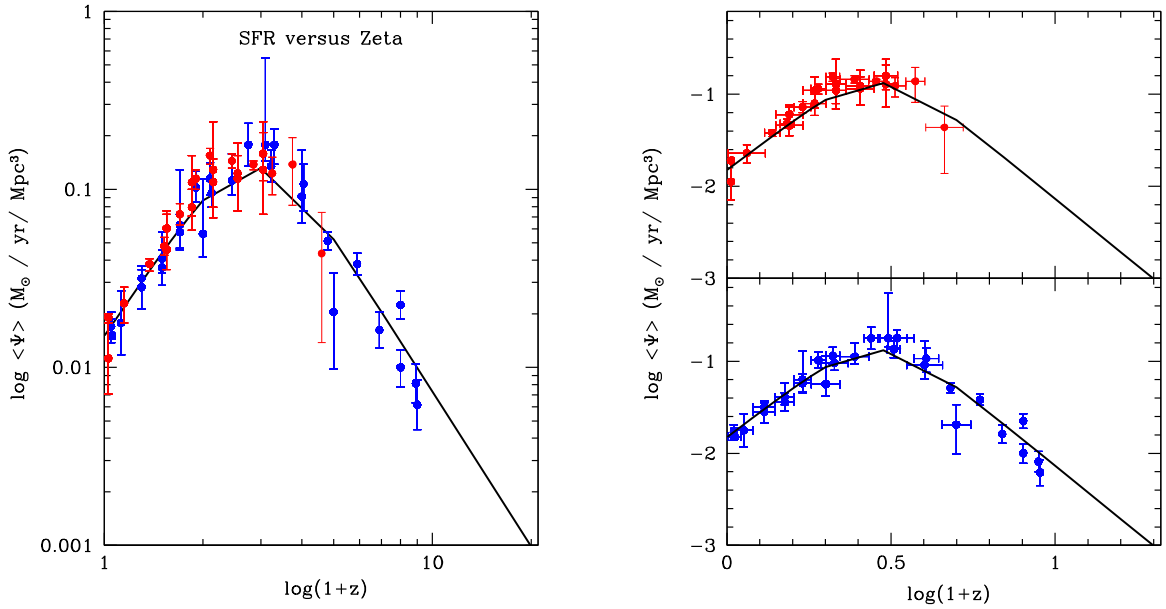

Figure 1. History of cosmic star formation according to Madau & Dickinson (2014; their Figure 8). The left panel shows the rest-frame FUV+IR data (blue and red dots, respectively), whereas in the right panels, the same data are plotted separately. The sources of data are those listed in Table 1 of Madau & Dickinson (2014). The solid line in the three panels is the analytical best fit of the data given by Madau & Dickinson (2014).

Analytical fits. In this work, we make use of the analytical fits derived by Madau & Dickinson (2014) and Madau & Fragos (2017). Both have similar functional dependencies that are given by

$$\mathrm{SFRD(z)} = \gamma_0 \frac{(1+z)^{\gamma_1}}{1+\left(\frac{1+z}{\gamma_2}\right)^{\gamma_3}}\, M_\odot\ \mathrm{yr}^{-1}\mathrm{Mpc}^{-3}. \quad (1)$$

The relation of Madau & Dickinson (2014) is for $\gamma_0 = 0.015$, $\gamma_1 = 2.7$, $\gamma_2 = 2.9$, and $\gamma_3 = 5.6$, and it is shown in the three panels of Figure 1 together with the original data from the same source.

The above relationship has recently been slightly revised by Madau & Fragos (2017), who used the Kroupa (2001) IMF. The new coefficients and exponents are $\gamma_0 = 0.01$, $\gamma_1 = 2.6$, $\gamma_2 = 3.2$, and $\gamma_3 = 6.2$. It is easy to check that the old and new relationships agree within a factor of about two. Both represent the footprint of the past star and galaxy formation history of the Universe that needs to be deciphered (see Figure 19 for a comparison).

3. Strategy: Deriving the SFRD(z) from Fundamental Building Blocks

In this study, we intend to derive the observational SFRD(z) from a small number of hypotheses or "building blocks":

(1) The cosmic scenario and the hierarchical building-up of bound structures that provide the number density of DM halos of mass $M_{\rm DM}$ and radius $R_{\rm DM}$ as a function of the redshift, $N(M_{\rm DM},z)$.
(2) The aggregation of BM in DM halos, which provides the visible component of galaxies and their star formation and chemical enrichment. This gives rise to a complicate interaction among several important physical processes, chief among others the gravitational contraction and collapse, together with gas heating and cooling and star formation. All this requires a suitable timescale to occur, so that the building-up of the stellar component of a galaxy cannot be instantaneous. The best simple model to describe this situation is the so-called "infall model" developed by Chiosi (1980).
(3) The spectro-photometric properties of the stellar population of galaxies that will provide the evolution of the spectral energy distribution as function of time, SFH, and chemical enrichment. This gives us magnitudes and colors of the stellar populations in galaxies as a function of the time and/or redshift for any photometric system in use.

The SFRD(z) results from combining the building blocks above: at each redshift, we know the number density of DM halos and associated BM galaxies born in the redshift $z_f \leqslant z$, where z_f is the redshift at which the first galaxies are assumed to form ($z = 20$ in our case). At each redshift, we calculate the number density of galaxies per Mpc^3 as a function of the mass of the DM halo (this soon sets the mass of the BM galaxy hosted by a DM halo). For this ideal sample of galaxies, we calculate the total and mean cosmic density of star formation, metallicity, mass in stars, and luminosity that is emitted in any passband according to

$$[\mathcal{F}]_T = \int\int \mathcal{F}(M_{\rm DM}, z, z_f) \times N(M_{\rm DM}, z, z_f) dM_{\rm DM} dz \quad (2)$$

$$\langle \mathcal{F} \rangle = \frac{\int\int \mathcal{F}(M_{\rm DM}, z, z_f) \times N(M_{\rm DM}, z, z_f) dM_{\rm DM} dz}{\int\int N(M_{\rm DM}, z, z_f) dM_{\rm DM} dz}, \quad (3)$$

where $\mathcal{F}$ stands for any of the physical quantities listed above, and the integrals are carried out over the range of $M_{\rm DM}$ and $z_f \geqslant z \geqslant 0$ we have considered. The correspondence between the halo mass $M_{\rm DM}$ and the BM galaxy mass $M_{\rm BM}$ inside is fixed by the cosmological model of the Universe (see below).

Table 1
Coefficients of the Polynomial Interpolation of Relation (4), which Provides the Number Density of Halos $N(M_{\rm DM}, z)$ per (Mpc/h)^3

Mass $[M_\odot/h]$	A_4	A_3	A_2	A_1	A_0
5e7	−2.34275e–5	1.28686e–3	−2.97961e–2	2.11295e–1	2.02908
5e8	−2.76999e–5	1.49291e–3	−3.47013e–2	2.13274e–1	1.13553
5e9	−1.31118e–5	6.50876e–4	−2.36972e–2	1.31993e–1	0.23807
5e10	−1.18729e–5	6.65488e–4	−3.17079e–2	1.30360e–1	−0.59744
5e11	−1.47246e–5	8.10097e–4	−4.65279e–2	1.13790e–1	−1.44571
5e12	6.59657e–5	−7.19134e–4	−6.99445e–2	1.06782e–1	−2.45684
5e13	−7.34568e–4	9.99022e–3	−1.65888e–1	−9.48292e–2	−3.11701

4. First Building Block: Number of DM Halos at Different Redshifts

We assume the Λ-CDM concordance cosmology, with values inferred from the *WMAP*-5 data (Hinshaw et al. 2009): flat geometry, $H_0 = 70.5\,{\rm km\,s^{-1}\,Mpc^{-1}}$, $\Omega_\Lambda = 0.72$, $\Omega_m = 0.28$, $\Omega_b = 0.046$ (giving a baryon ratio of $\Omega_b/\Omega_m \simeq 0.1656$), $\sigma_8 = 0.817$, and $n = 0.96$. To these values for Ω_m and Ω_b we have the corresponding ratio between the baryonic and dark matter masses of individual galaxies $M_{\rm BM}/M_{\rm DM} \simeq 0.16$ and vice versa $M_{\rm DM}/M_{\rm BM} \simeq 6.12$.

As already mentioned, the standard approach to investigating the cosmic SFRD is based on large-scale cosmological N-body simulations in the framework of a given cosmological model of the Universe (Λ-CDM in our case), so that the appearance, growth, and subsequent aggregation of perturbations of all scales can be suitably described (e.g., Springel et al. 2005b). The formation of DM halos and BM galaxies inside are automatically taken into account in the simulations. The price to pay is a high computational cost, so that the analysis is limited to a few paradigmatic cases.

As an alternative, one may adopt the strategy used by Lukić et al. (2007). Starting from the Warren et al. (2006) halo mass function (HMF), they derive the halo growth function (HGF) in the concordance Λ-CDM model over a wide range of redshifts (from $z \simeq 20$ to the present; see their Figure 2). The HGF $N(M_{\rm DM}, z)$ gives the number density of halos of different masses per (Mpc h^{-1})^3 resulting from all creation/destruction events. By performing a large suite of nested-box *N*-body simulations with careful convergence and error controls, they determine the mass function and its evolution with excellent statistical and systematic errors, reaching a few percent over most of the considered redshift and mass range. The advantage of the Lukić et al. (2007) study is that it provides a halo mass distribution function, $N(M_{\rm DM}, z)$, that is easy to use in all cases, like our case here, in which galaxy evolution has to be framed in a cosmological context.

In order to make use of the Lukić et al. (2007) distribution in our analysis, we fit their results with a fourth-order polynomial

$$\log N(M_{\rm DM}, z) = \sum_{j=0}^{4} A_j(M_{\rm DM}) \times z^j. \quad (4)$$

The coefficients $A_j(M_{\rm DM})$ are listed in Table 1. The interpolated distribution function for the number density $N(M_{\rm DM}, z)$ of halos per Mpc^3 as a function of the mass and redshifts is shown here in Figure 2, and the associated number densities are in Table 2. As expected, it is identical to the original function by Lukić et al. (2007).

Although the following is well known, see the pioneer study of Press & Schechter (1974) and Lukić et al. (2007, for ample referencing), for the sake of clarity and relevance for our discussion, we note the following: (i) for each halo mass (or mass interval), the number density is low at high redshift, increases to high values toward the present, and depending on the halo mass, either reaches a maximum value at a certain redshift followed by a decrease (typical of low-mass halos), or continues to increase, as in the case of high-mass halos; in other words, first the creation of halos of a given mass (by spontaneous growth of perturbation to the collapse regime or by mergers) overwhelms their destruction (by mergers), whereas the opposite occurs past a certain value of the redshift for low-mass halos; (ii) at any redshift, high-mass halos are orders of magnitude less frequent than low-mass halos; (iii) at any redshift, the mass distribution of halos has a typical interval of existence whose upper mass end (cut-off mass) increases at decreasing redshift.

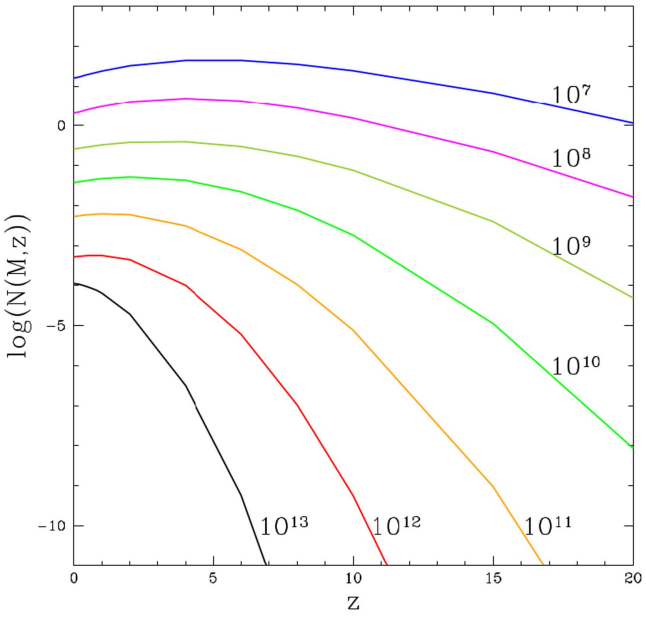

Figure 2. HGF reproduced from Lukić et al. (2007). The number density of galaxies (in logarithmic scale) is given in (Mpc h^{-1})^3, where $h = H_0/100$. Each line refers to halos with DM mass in solar units, as indicated.

Finally, it is worth recalling that both the number densities $N(M_{\rm DM}, z)$ of Lukić et al. (2007) and the SFRD(z) of Madau & Dickinson (2014) are per Mpc^3, so that comparing theory with observations is less of a problem. However, owing to the many uncertainties affecting the observational data and the crudeness of the theoretical models, small adjustments on the order of a few units can be tolerated in the final comparison.

5. Second Building Block: the BM Galaxies Inside DM Halos

Given the mass distribution of DM halos as a function of the redshift and knowing the mass $M_{\rm BM}$ of baryons inside thanks to

the cosmological proportions $M_{\rm BM}/M_{\rm DM} \simeq 0.16$, one needs a prescription to form a model galaxy out of this lump of matter. DM and BM undergo gravitational collapse, baryons cool down, accumulate toward the core, and form stars. The visible galaxy is gradually built up. The timescale needed to arrive at the stage of nearly complete generation of the stellar content extends from the typical free-fall time (about 0.5 Gyr) to significantly longer than this (about 2 Gyr or even longer) depending on the galaxy type (mass). The NB-TSPH simulations of Chiosi & Carraro (2002) in a monolithic-like scheme and those of Merlin & Chiosi (2006, 2007) and Merlin et al. (2012) in the early hierarchical scheme show that at decreasing galaxy mass, the SFR shifts from a single prominent early episode to ever continuous bursting-like mode as the galaxy mass and/or the overdensity of the initial perturbation decreases, and that in massive and intermediate-mass galaxies (with $M_{\rm BM}$ from 10^{10} to $10^{11}\,M_{\odot}$ or more) the building-up of the stellar component is complete up to 90% or so before $z \simeq 2$. These overall trends and timescales of galaxy formation have been found independently and were confirmed by Thomas et al. (2005) from their analysis of the line absorption indices in a large sample of galaxies. See also the review of Renzini (2006).

The infall models of galactic chemical evolution over the years have reached a very high degree of complexity and sophistication, have been applied to study galaxies of different morphological type going from early types to disks and irregulars, and have proved to successfully explain many observational properties of galaxies, such as chemical abundances, gas and stellar content, and, with the aid of photometric synthesis tools, magnitudes and colors as well. The situation has been widely reviewed by Matteucci (2012, 2016): we limit ourselves to mention here the models developed by Bressan et al. (1994), Chiosi et al. (1998), and Tantalo et al. (1996, 1998) for early-type galaxies, and by Portinari & Chiosi (1999, 2000) and Fattore (2009) for spherical and disk galaxies with radial flows of gas.

In the following, we use models that are adapted to the one-zone description (fully adequate to our purposes) from those elaborated by Tantalo et al. (1998) in spherical symmetry. Over the years, many important physical phenomena have been incorporated in the chemical models, for instance, gas heating by supernova explosions (both type II and type Ia); stellar winds; gas cooling by radiative emission, in order to correctly evaluate the thermal content of the gas eventually triggering the galactic winds; and finally, the radial flows of gas. The same physical processes have also been included in the *N*-body simulations of galaxy formation and evolution only recently. Owing to the scarce communication between the two scientific communities, the strong predicting power of the costless chemical models with respect to highly time-consuming numerical simulations has been ignored.

The essence of all infall models is the assumption of the gas accretion into the central region of the proto-galaxy at a suitable rate (driven by the timescale τ) and of gas consumption by a Schmidt-like law of star formation. The gas accretion and consumption combined give rise to a time dependence of the SFR that closely resembles the dependence resulting from the *N*-body simulations and the line absorption indices diagnostics. We return to this important issue below.

In the framework of infall models, the luminous mass $M_{\rm BM}$ increases with time according to

$$\frac{dM_{\rm BM}(t)}{dt} = \dot{M}_{\rm BM,0}\,\exp(-t/\tau), \tag{5}$$

where τ is the accretion timescale. The constant $\dot{M}_{\rm BM,0}$ is obtained from imposing that at the galaxy age T_G the value $M_{\rm BM}(T_G)$ is reached:

$$\dot{M}_{\rm BM,0} = \frac{M_{\rm BM}(T_G)}{\tau[1 - \exp(-T_G/\tau)]}, \tag{6}$$

Therefore, integrating the accretion law the time dependence of $M_{\rm BM}(t)$ is

$$M_{\rm BM}(t) = \frac{M_{\rm BM}(T_G)}{[1 - \exp(-T_G/\tau)]}[1 - \exp(-t/\tau)], \tag{7}$$

The above formalism allows us to immediately recover the *closed-box* approximation, letting $\tau \rightarrow 0$. The timescale τ parameterizes the timescale over which the present-day mass $M_{\rm BM}(T_G)$ is reached. In this scheme the total mass of a galaxy at the present time is $M_G = M_{\rm DM} + M_{\rm BM}(T_G)$.

5.1. Basic Equations of the Model

We denote with $X_i(t)$ the current mass abundance of an element i and introduce the dimensionless variables

$$G(t) = M_g(t)/M_{\rm BM}(T_G) \tag{8}$$

and

$$G_i(t) = G(t)X_i(t), \tag{9}$$

where by definition $\Sigma_i X_i(t) = 1$.

The equations governing the time variation of the $G_i(t)$ and hence $X_i(t)$ are

$$\frac{dG_i(t)}{dt} = -X_i(t)\psi(t) + \left[\frac{dG_i(t)}{dt}\right]_{\rm star} + \left[\frac{dG_i(t)}{dt}\right]_{\rm inf} - \left[\frac{dG_i(t)}{dt}\right]_{\rm win}, \tag{10}$$

where $\psi(t)$ is the normalized rate of star formation to be defined, and t is the current galaxy age.

The four terms at the right-hand side are in the following order: the rate of gas consumption by star formation, the rate of gas restitution (ejecta) by stars formed in previous epochs, the rate of mass accretion by infall of primordial gas onto the system, and the finally, the rate at which enriched gas leaves the system. The infall rate is given by

$$\left[\frac{dG_i(t)}{dt}\right]_{\rm inf} = \frac{X_{\rm inf}}{M_{\rm BM}(T_G)}\left[\frac{dM(t)}{dt}\right]_{\rm inf}, \tag{11}$$

and it is easily derived from Equation (5). The rate of gas ejection is formally given by

$$\left[\frac{dG_i(t)}{dt}\right]_{\rm win} = \frac{X_i(t)}{M_{\rm BM}(T_G)}\left[\frac{dM(t)}{dt}\right]_{\rm win} \tag{12}$$

and is usually taken to be very high (nearly instantaneous ejection of all heated up gas).

The rate of gas ejection by stars is more complicated to calculate. The correct definition of this quantity can be found in Bressan et al. (1994), Tantalo et al. (1996), and Tantalo et al. (1998). Suffice it here to mention that (i) it requires integration over the IMF to account for the different contribution from stars of different mass and lifetime τ_M, (ii) the stellar yields are calculated according to the so-called Q-formalism (cf. Talbot & Arnett 1971, 1973); (iii) at any age t, the rate of star $\psi(t)$

weighting the contribution from star of different mass M must be evaluated at $t_M = t - \tau_M$. The inclusion of Type Ia supernovae is made according to Matteucci & Greggio (1986), and it requires the specification of the mass interval and mass ratios for the binary star progenitors of Type Ia supernovae together with the distribution function $f(\mu)$ of their mass ratios and the percentage of such binary systems with respect to the total. The contribution from Type II supernovae is straightforward, and it is incorporated in the Q-formalism. The stellar ejecta are taken from Marigo et al. (1996, 1998), Portinari (1998), and Portinari et al. (1998), to whom we refer for all details. The stellar lifetimes τ_M are adopted from the tabulations by Bertelli et al. (1994) and take the dependence of τ_M on the initial chemical composition into account. Finally, for the purposes of this study, we follow in detail only the total metallicity (the sum of the abundances by mass of all elements heavier than ^{4}He), shortly indicated by $Z = \sum_{j>\mathrm{He}} X_j$.

Last, we write the equation for the current mass of a galaxy in the form of stars $M_s(t)$: at any age t, this is given by

$$M_s(t) = M_{\mathrm{BM}}(t) - M_g(t) \tag{13}$$

with obvious meanings of the symbols.

5.2. The Stellar Initial Mass Function

For this we choose the Salpeter (1955) law by number

$$\phi(M) = M^{-x}, \tag{14}$$

where $x = 2.35$. The IMF is normalized by choosing the fraction ζ of stars more massive than M_n, i.e., the mass interval that contributes most to chemical enrichment over the whole Hubble time,

$$\zeta = \frac{\int_{M_n}^{M_u} \phi(M) \times M \times dM}{\int_{M_l}^{M_u} \phi(M) \times M \times dM}, \tag{15}$$

where M_u and M_n are fixed and equal to $M_u = 100\,M_\odot$ and $M_n \simeq 1\,M_\odot$, the lowest mass limit M_l is left free. Following Bressan et al. (1994) and Tantalo et al. (1996, 1998), good choices force for ζ are from 0.3 to 0.5 (and the values for M_l are consequently derived).

5.3. The Star Formation Rate

The rate of star formation is assumed to depend on the gas mass according to

$$\Psi(t) = \frac{dM_g}{dt} = \nu M_g(t)^k, \tag{16}$$

where ν and k are adjustable parameters.

The SFR normalized to $M_{\mathrm{BM}}(T_G)$ becomes

$$\psi(t) = \nu M_{\mathrm{BM}}(T_G)^{k-1} G(t)^k. \tag{17}$$

Linear and quadratic dependencies of the SFR on the gas content, $k = 1$ and $k = 2$, respectively, were first proposed by Schmidt (1959) and have been adopted ever since because of their simplicity (see Larson 1991, for a classical review of the subject). We adopt here $k = 1$.

With the law of star formation of Equation (16), the resulting time dependence of $\psi(t)$ is driven by the rate of mass accretion onto the system. In the closed-box description, the SFR is maximum at the beginning, and after this, it continuously decreases until galactic winds occur. In the infall model, owing to the competition between the rate of gas infall and gas consumption by star formation, the rate of star formation starts low, increases to a maximum, and then declines. The age at which the peak occurs, shortly indicated by T_P, approximately corresponds to the infall timescale τ.

Finally, ν is the efficiency parameter of the star-forming process. Its physical meaning is better understood by casting the SFR in a slightly different fashion. One can identify dt with the timescale τ of the mass accretion rate and assume $k = 1$,

$$\Psi(t) = \frac{dM_g}{dt} = \nu M_g(t)^k \Rightarrow \frac{\Delta M_g}{M_g} = \tau\,\nu \Rightarrow \simeq \frac{\Delta M_s}{M_g} = \tau\,\nu, \tag{18}$$

where the ratio $\Delta M_s/M_g$ is the mass of gas already converted into stars with respect to the mass of the left-over gas. Furthermore, if the accretion τ is identified with the infall timescale t_{ff} of a galaxy, we may obtain rough estimates of the specific star formation efficiency. The infall timescale of a galaxy can be approximated to the collapse timescale of primordial perturbations, which depends on the redshift but is independent of the galaxy mass. Rough estimates of τ yield values ranging from 0.05 to 0.1 Gyr when the galaxy formation redshift is in the interval 20 to 1. This in turn implies $\nu \simeq 20$ to 1 to assemble a typical $10^{12}\,M_\odot$ galaxy. This efficiency is lowered by a factor of 10 at least if the mass assembly is diluted over the Hubble time.

According to Cassarà et al. (2016), the shape of SFR as a function of time can be schematically grouped according to the value taken by the ratio of the two parameters τ and ν (see Figure 2 of Cassarà et al. 2016). With the above laws of gas accretion and star formation, they are able to model two main types of objects: (i) in bulge-like models, characterized by high values of ν and low values of τ (ratios $\tau/\nu \leqslant 0.1$), the SFR increases to a peak on a relatively short timescale (on average 0.5 Gyr), and soon after declines. These models reproduce the chemical pattern in the gas of early-type galaxies at both low (Piovan et al. 2006a, 2006b, 2006c; Pipino & Matteucci 2011) and high redshift (e.g., Matteucci & Pipino 2002; Pipino & Matteucci 2011); (ii) in the disk-like models, characterized by low values of ν together with high values of τ (ratios $\tau/\nu \geqslant 1$), the SFR shows a slow rise followed by a slow decline. These models could well mimic disk and to some extent also irregular galaxies in the local Universe (Piovan et al. 2006a, 2006b, 2006c; Pipino et al. 2013).

Finally, we would like to mention that a functional form for the SFR that could mimic the above systematic variation with galaxy type (mass) is the so-called delayed exponentially declining law,

$$\Psi(t) \propto \frac{t}{\tau} \exp\left(-\frac{t}{\tau}\right). \tag{19}$$

In this framework, the Schmidt law is the link between the gas accretion by infall and the gas consumption by star formation. By varying the parameters τ and ν, we may model different types of galaxies (Buzzoni 2002).

Based on these considerations and taking the results of NB-TSPH simulations by Chiosi & Carraro (2002), Merlin & Chiosi (2006, 2007), and Merlin et al. (2012) as reference

templates for the SFH in galaxies of different mass and morphological types, we calculate chemical models for different combinations of τ and ν that are meant to cover the whole Hubble sequence of galaxies.

5.4. Onset of Galactic Winds: Energy Feedback and Gas Heating-cooling

Larson (1974) postulated that the present-day color-magnitude relations of elliptical galaxies (see Bower et al. 1992; Kodama et al. 1999, 2001; Terlevich et al. 2001, and references) might be the result of galactic winds powered by supernova explosions, thus initiating a long series of chemo-spectro-photometric models of elliptical galaxies that were based on this idea (Saito 1979a, 1979b; Arimoto & Yoshii 1987; Matteucci & Tornambé 1987; Angeletti & Giannone 1990; Matteucci 1994; Mihara & Takahara 1994; Gibson & Matteucci 1997; Gibson 1998, and references therein). In brief, gas is let escape from the galaxy, and star formation is assumed to halt when the total thermal energy of the gas equates its gravitational binding energy. The same scheme is adopted here in the models that take galactic winds into account, i.e., the term $\left[\frac{dG_i(t)}{dt}\right]_{\rm win}$ in Equation (10) is at work.

The thermal energy of the gas is mainly due to three contributions, namely Type Ia and II supernovae, and stellar winds from massive stars:

$$E_{\rm th}(t) = \sum_J E_{\rm th}(t)_J, \tag{20}$$

where $J \equiv$ SNI for Type Ia supernovae, $J \equiv$ SNII for Type II supernovae, and $J \equiv W$ for stellar winds; each term has a similar dependence

$$E_{\rm th}(t)_J = \int_0^t \epsilon_J(t - t')R_J(t')M_{\rm BM}(T_G)dt' \tag{21}$$

with obvious meaning of the symbols. The quantities $\epsilon_J(t - t')$ and $R_J(t)$ are the energies emitted by a supernova and/or stellar wind event and the corresponding production rates, respectively. As the production rates are functions of the dimensionless variables $G_i(t)$, the normalization factor $M_{\rm BM}$ is required to calculate the energy in physical units. The production rates can be easily derived from the equations governing the chemical evolution. The emitted energies incorporate the cooling laws of supernova remnants and stellar winds by radiative cooling processes according to expression used by Tantalo et al. (1998).

Finally, star formation and chemical enrichment of the model galaxies are halted, and the remaining gas is assumed to be expelled (winds) when the condition

$$E_{\rm th}(t) \geqslant |\Omega_g(t)| \tag{22}$$

is verified.

5.5. Gravitational Potential of DM and BM

To calculate the gravitational energy of the gas, we make use of the analytical dynamical models of Bertin et al. (1992) and Saglia et al. (1992) and adapt them to our case. DM is assumed to be already in situ, whereas the BM is assumed to fall into the gravitational well of the former and soon to reach the equilibrium configuration, so that at each instant, the description of Bertin et al. (1992) and Saglia et al. (1992) can be applied. In this description of galactic structure, the mass and radius of the DM, $M_{\rm DM}$ and $R_{\rm DM}$, respectively, are related to those of the BM, $M_{\rm BM}$, and $R_{\rm BM}$ by the relation

$$\frac{M_{\rm BM}(t)}{M_{\rm DM}} \geqslant \frac{1}{2\pi}\left(\frac{R_{\rm BM}(t)}{R_{\rm DM}}\right)\left[1 + 1.37\left(\frac{R_{\rm BM}(t)}{R_{\rm DM}}\right)\right], \tag{23}$$

and the binding gravitational energy of the gas is given by

$$\Omega_g(t) = -\alpha_{\rm BM}G\frac{M_g(t)M_{\rm BM}(t)}{R_{\rm BM}(t)} - G\frac{M_g(t)M_{\rm DM}}{R_{\rm BM}(t)}\Omega'_{\rm BDM} \tag{24}$$

where G is the gravitational constant, $M_g(t)$ is the current value of the gas mass, $\alpha_{\rm BM}$ is a numerical factor $\simeq$0.5, and

$$\Omega'_{\rm BDM} = \frac{1}{2\pi}\left(\frac{R_{\rm BM}(t)}{R_{\rm DM}}\right)\left[1 + 1.37\left(\frac{R_{\rm BM}(t)}{R_{\rm DM}}\right)\right] \tag{25}$$

is the contribution to the gravitational energy given by the presence of DM. According to Bertin et al. (1992) and Saglia et al. (1992), in equilibrium conditions, $M_{\rm BM}/M_{\rm DM} \simeq R_{\rm BM}/R_{\rm DM}$. With the current estimates of $M_{\rm DM}$ and $M_{\rm BM}$ of the Λ-CDM cosmogony both ratios are equal to 0.16. With these values, the factor $\Omega'_{\rm BDM} = 0.04$, so that the total correction to the gravitational energy of the gas (Equation (24)) does not exceed 0.3 of the term for the luminous mass.

5.6. General Remarks on the Galactic Models

Mass homology. It is worth noting that with the above formalism, all the models are *homologous in mass* in the absence of galactic winds in the sense that the same solution (current fractional gas and star mass) applies to galaxies of different mass provided it is suitably rescaled to the total asymptotic baryonic mass, i.e., the total baryonic mass reached at $t = T_G$. The same technique can also be used in the presence of galactic winds by suitably rescaling the asymptotic mass to the real value, i.e., subtracted by the amount of gas mass that is definitely lost by the system in the form of galactic winds.

Specific star formation rate. It is also worth noting that with above assumptions, the SFR in use is the specific star formation rate (SFR per unit baryonic mass, SSFR), which depends on three parameters, i.e., ν, τ, and T_P. Since τ and T_P are correlated, each galaxy model here is characterized only by the parameters ν and τ.

Groups of galaxy models. For the purposes of this study, we have calculated three groups of models, labeled A, B, and C.

Group A. In the models of group A, we assume that all galaxies begin their evolutionary history at redshift $z = 20$ and assume that the mass accretion timescale τ corresponds to the free-fall timescale for the ρ_{200} overdensity of the proto-galaxy with respect to the surrounding medium at this value of the redshift. The free-fall timescale is given by

$$t_{ff}(z) = \sqrt{\frac{3\pi}{32G\rho_{200}}} \tag{26}$$

for the homologous collapse of a homogeneous sphere of gas. This timescale is the same for all galaxies independently of their mass. The free-fall timescale $t_{ff}(z)$ extends from about 3.5×10^7 years at $z = 20$ to about 1.0×10^9 years at $z = 1$.

For the star formation efficiency parameter ν, we adopt the constant value $\nu = 10$. Owing to the very short mass accretion

timescale and high value of ν, these models are very similar to the ideal situation of the closed-box approximation. The baryonic mass of the models spans the range 10^7 to $10^{12}\,M_\odot$.

Group B. In light of the considerations on the type of SFH in real galaxies, in models of group B we adopt values for the accretion timescale τ ranging from 6 Gyr to 2 Gyr as the baryonic mass increases from $10^7\,M_\odot$ to $10^{12}\,M_\odot$, but keep the value for the parameter ν unchanged, i.e., $\nu = 10$ for all the models. Since the ratio τ/ν of the models of groups A and B is always lower than one, they are best suited to represent early-type objects of any mass from dwarfs to bulges and massive ellipticals (Cassarà et al. 2016).

Group C. Finally, the models of Group C more closely follow the classification by Cassarà et al. (2016), who rank the galaxy SFR by means of the ratio τ/ν. First of all, we stretch the interval of the accretion timescale τ assigned to each BM mass. It now extends from 2 Gyr for the $M_{\rm BM} = 10^{12}\,M_\odot$ galaxy to 10 Gyr for the $M_{\rm BM} = 10^7\,M_\odot$. Second, for each value of τ, we explore three values of ν, namely $\nu = 0.1$, 1, and 10. In this way, we can model galaxies along the whole Hubble sequence by varying the ratio τ/ν depending on the galaxy mass: low values for the most massive galaxies correspond to massive early types, intermediate values for the less massive galaxies (from intermediate early type to massive spirals), and high values for the less massive galaxies such as low spirals and irregulars. Group C partially overlaps group B.

Other combinations of two out of the three parameters (τ, ν, and hence τ/ν) are of course possible. Since the aim here is to calculate galaxy models whose SFR and SFH closely resemble those observed in real galaxies, the choice we have made is fully adequate to our purposes.

Finally, we like to point out that the models of Group A are meant to represent a sort of reference sample corresponding to the ideal situation of the closed-box approximation. They are used only to evaluate the effects on the SFRD(z) of an exponentially decreasing rate of star formation.

Table 3 lists all the parameters adopted for the chemical models.

5.7. Results for the Chemical Models

The model galaxies are calculated from $z_f = 20$ to $z = 0$, i.e., from the rest-frame age $t = 0$ Gyr to the maximum age of $T_G = 13.75$ Gyr, where $T_G = t_u(z = 0) - t_u(z = z_f)$, with $t_u(z)$ being the age of the Universe for the adopted cosmological model.

If for any reason we need to change the redshift of galaxy formation from z_f to $z_f^* \leqslant z_f$ (keeping all other input parameters unchanged), the same models can be used provided their rest-frame age is simply limited to the interval from $t = 0$ at z_f^* to $T_G^* = T_{G,(z_f=20)} - t_u(z_f^*)$, where $t_u(z_f^*)$ is the age of the universe at $z = z_f^*$. In other words, at $z = 0$, the new galaxy is younger than the previous one.

In this first step of the analysis, the occurrence of galactic winds is not considered on purpose. This means that the energy input from Type II and Type Ia supernovae and galactic winds is turned off so that star formation can occur throughout the life of galaxies.

Finally, the discussion below is limited to the models of case B. Those of cases A and C have similar trends and behavior.

Star formation. The specific (in units of yr^{-1}) and true star formation (in $M_\odot\ \mathrm{yr}^{-1}$) of the model galaxies are shown in the left and right panels of Figure 3. As expected, the SSFRs look very similar to each other, whereas the true rates may significantly change with galaxy mass. From now on, different values of M_G are identified in all figures with the following colors: blue ($10^7\,M_\odot$), magenta ($10^8\,M_\odot$), olive green ($10^9\,M_\odot$), green ($10^{10}\,M_\odot$), orange ($10^{11}\,M_\odot$), and red ($10^{12}\,M_\odot$).

Metallicity. The temporal variation of the metallicity Z for the model galaxies is shown in Figure 4. Owing to the rather high value of ν and parameter ζ of the IMF normalization, high metallicites are built up in the galaxies. This is less of a problem because by lowering ν and/or ζ, one would obtain similar results but lower values of the metallicity at the present time, without changing the overall behavior of the solution.

Gas and star contents. Finally, in Figure 5 we show the temporal variation of the fractional masses of gas (bottom panel) and stars (top panel) for the models of group B. The timescale of mass accretion varies with the galaxy mass, as reported in Table 3. The intrinsic efficiency of star formation is the same for the models we show (i.e., $\nu = 10$). Because of the high efficiency of star formation, all the models have the peak of activity within the first Gyr of their lifetime.

The role of ν. In concluding this section, it is worth commenting on the role of the intrinsic efficiency ν in shaping the final time-dependence of the SFR in infall models of galaxy formation and evolution. So far, the discussion of the results for groups B and C has been limited to models with efficient SFR, represented here by all the cases with $\nu = 10$. The peak of activity is always confined to within the first Gyr. Clearly, for $\nu = 10$, case C does not differ too much from case B. We give preference to this particular choice for the parameter ν in view of the discussion below concerning the SFRD(z).

It is worth emphasizing that the role of ν is of paramount importance in shaping the overall time-dependence of the SFR. The situation is best illustrated in Figure 6, which displays the SFR versus time of the $1 \times 10^{12}\,M_\odot$ and $1 \times 10^8\,M_\odot$ galaxies of Group C (three values of ν for each case). The models gradually change their SFR from early peaked to ever-continuing according to the value of the ratio τ/ν, in other words, along the Hubble sequence of galaxies passing from early types (low ratios τ/ν) to disk-like objects (intermediate ratios τ/ν), and finally to irregulars (high ratios τ/ν). This trend of the star formation was suggested by Sandage (1986), from examining the SFR in galaxies of different types, and has more recently been confirmed by studies of SFHs based on absorption line indices by Thomas et al. (2005) and NB-TSPH numerical models of galaxy formation and evolution (Chiosi & Carraro 2002; Merlin et al. 2012).

5.8. Remarks on the Star Formation Rate

As already mentioned, the time dependence of our SFR is the delayed exponential law, see Equation (19), which is implicit to the galactic chemical models with gas accretion. The reasons why the simple exponential law,

$$\Psi(t) \propto \frac{1}{\tau}\exp\left(-\frac{t}{\tau}\right), \tag{27}$$

adopted previously by Tinsley (1972) and in usage even today, must be abandoned have been discussed many times (see the classical studies by Lynden-Bell (1975), Chiosi (1980), and the recent review by Matteucci (2016), so that they are not repeated here).

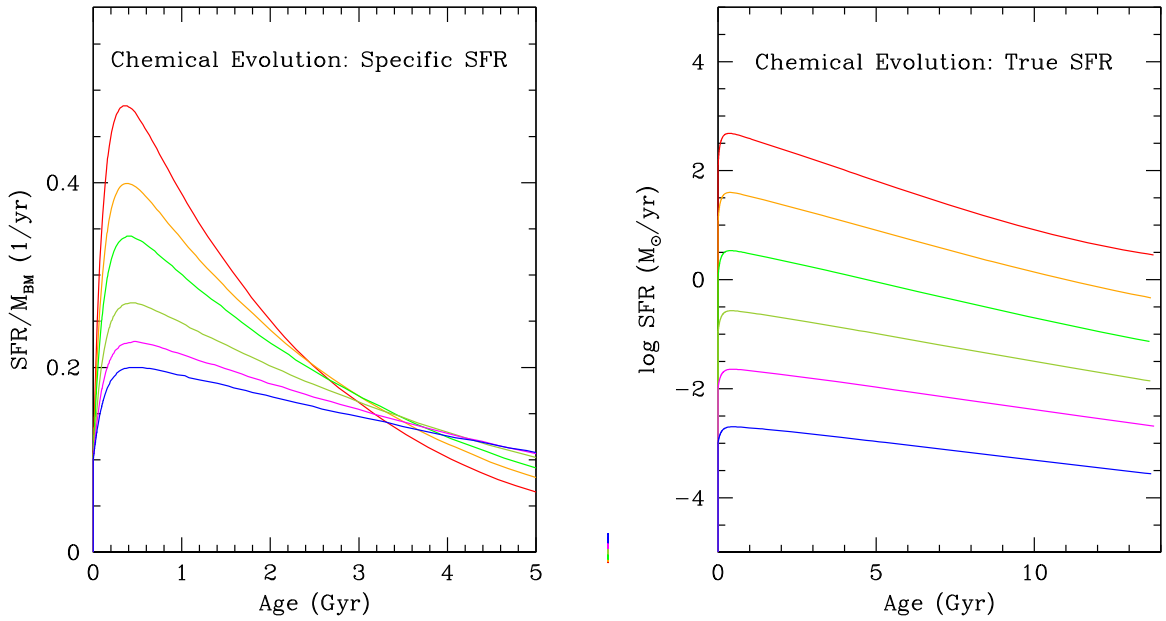

Figure 3. Left panel: SSFR of models B in yr^{-1} for galaxies of different M_{BM}, different accretion (collapse) timescale τ, and efficiency $\nu = 10$. The mass M_{BM} increases from 10^7 to $10^{12}\,M_\odot$ from bottom to top. No galactic winds are assumed to occur. The time is the age of the galaxy in the rest-frame. Right panel: same as in the left panel, but for the true SFR in units of $M_\odot\ yr^{-1}$.

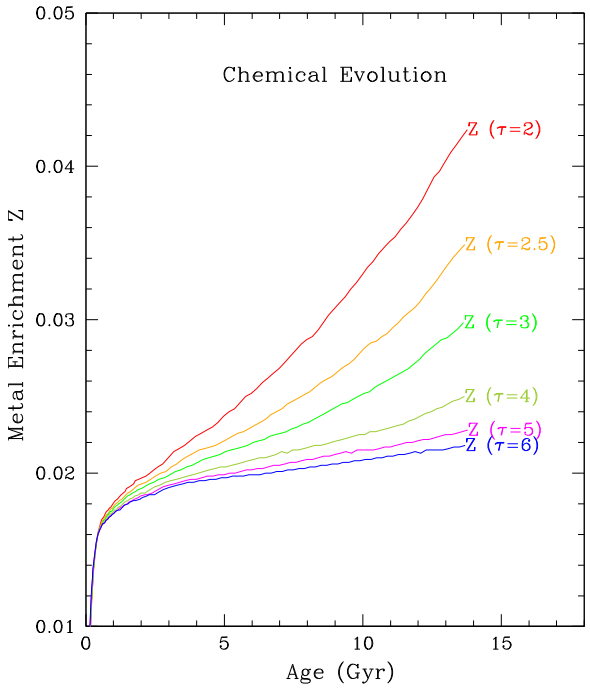

Figure 4. Metallicity vs. time relation for the galaxies of group B with different M_{BM}, different accretion timescale τ and efficiency $\nu = 10$. No galactic winds are assumed to occur. The mass M_{BM} incresases from 10^7 to $10^{12}\,M_\odot$ from bottom to top.

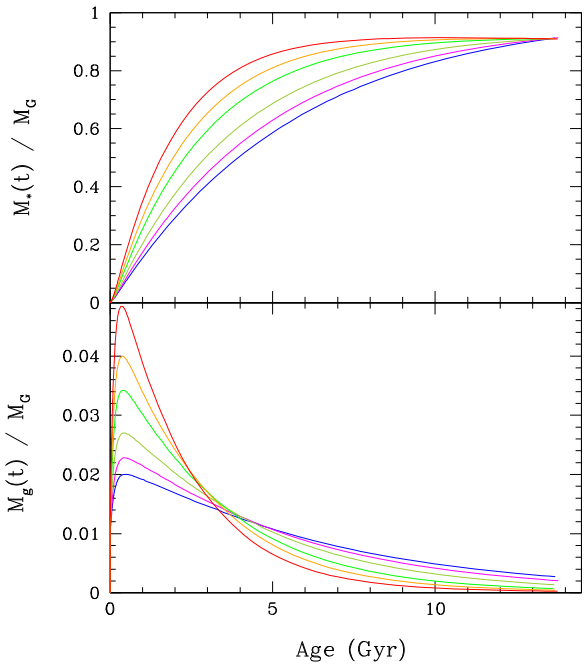

Figure 5. Gas and star content vs. time relationships for the galaxies belonging to group B with different M_{BM}, different accretion timescale τ, and efficiency $\nu = 10$. The mass M_{BM} increases from 10^7 to $10^{12}\,M_\odot$ from bottom to top.

In favor of the time-delayed exponential law were the original models by Chiosi (1980) and the long list of studies dedicated to the evolution of chemical elements in galaxies of different morphological type, extending from bulges and early-type objects to disk and even irregular galaxies (see Matteucci 2012, 2016, for exhaustive reviews and referencing of this issue). In support of the delayed exponential law is also the study of Gavazzi et al. (2002) with the spectro-photometric data of galaxies in the Virgo cluster.

These classical analytical representations of the SFR have recently been questioned by Oemler et al. (2013), who based their analyses on the SSFR in the redshift interval $z \leqslant 1$. They concluded that the standard laws cannot explain both the tail of high specific SFR at $z = 1$ and the low value we see today at $z = 0$. They also argued that the starbust hypothesis cannot solve the problem. Gladders et al. (2013) argued that a

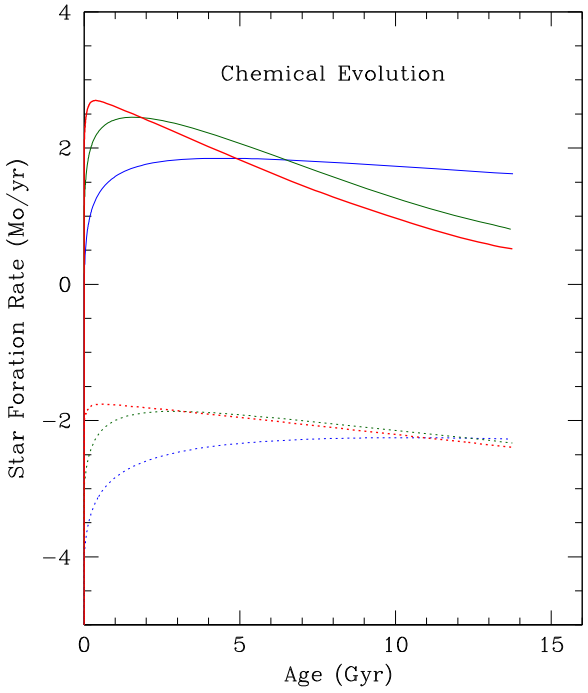

Figure 6. SFR vs. time relationship for the galaxies of different $M_{\rm BM}$ belonging to group C at varying τ and ν. Two values of the galaxy mass (baryonic component) are considered, namely $10^8\,M_\odot$ and $10^{12}\,M_\odot$. The values of τ and ν are listed in Table 3.

lognormal SFH of galaxies successfully describes both the SFRD over cosmic times and the present-day distribution of the SSFR of galaxies and the evolution of this quantity up to $z \simeq 1$. The lognormal SFR law they assumed is

$$\mathrm{SFR}D(t) \propto \frac{1}{t\tau}\exp\left[-\frac{(\ln(t)-T_0)^2}{2\tau}\right], \tag{28}$$

where T_0 and τ (not to be mistaken with the timescale of gas accretion in galaxies) are the cosmic SFRD half-mass time and width (in units of ln (time)). Based on the notion that lognormal laws seem to be ubiquitous in nature (Limpert et al. 2001), they took the SDSS sample of local galaxies (2094 objects), assigned them a lognormal SFR, and derived for each object the SFR (i.e., the parameters T_0 and τ), while ensuring that the ensemble of SFRs summed to the SFRD. Abramson et al. (2016) continued along this line of reasoning. Adding and combining many lognormal SFHs parameterized by T_0 and τ, they argued that this simple model reproduces (i) the stellar mass functions at $z \leqslant 8$; (ii) the slope of the SFR versus stellar mass relation (the galaxy main sequence) at $z \leqslant 6$; (iii) galaxy downsizing; (iv) and a correlation between the formation timescale and the SSFR(M_s,t).

In our view, the straight inference of a lognormal SFR in single galaxies contributing to the total cosmic SFRD is somewhat arbitrary and misleading. The cosmic SFRD is not the simple summation of that of many galaxy SFRs because each galaxy may differ from the others, nor do all types of galaxy occur in equal number, but it results from the number-weighted summation of many objects of different type and SFHs (see below). The SFR of a galaxy might not be lognormal and yet the cumulative effect of many of them may appear as a lognormal distribution. For these reasons, we prefer to describe the SFR of galaxies as independent entities with the time-delayed law.

6. Third Building Block: Photometry

The integrated monochromatic flux generated by the stellar content of a galaxy of age T is defined as

$$F_\lambda(T) = \int_0^T \Psi[t, Z(t)]\; sp_\lambda[\tau', Z(\tau')]\; dt, \tag{29}$$

where $\Psi[t, Z(t)]$ is the SFR at the current age t and metal content Z (chemical composition in general), $sp_\lambda[\tau', Z(\tau')]$ the integrated monochromatic flux of single stellar population (i.e., of a coeval, chemically homogeneous assembly of stars, named SSP) with age τ' and metallicity $Z(\tau')$, and finally $\tau' = T - t$. The flux of a SSP is in turn given by

$$sp_\lambda[\tau', Z(\tau')] = \int_{M_l}^{M_u} \phi(M)\, f_\lambda[M, \tau', Z(\tau')]\; dM, \tag{30}$$

where $\phi(M)$ is the stellar IMF and $f_\lambda(M, \tau', Z)$ the monochromatic flux of a star of mass M, metallicity Z, and age $\tau' = T - t$. M_l and M_u define the mass range within which stars are generated by each event of star formation. The metallicity dependence of the rate of star formation $\Psi(t, Z)$ is customarily neglected, and the same holds for the time and metallicity dependencies of the IMF.

The flux of an SSP, $sp_\lambda(\tau', Z)$, is calculated by integrating Equation (30) along an isochrone of age τ' populated by "virtual stars" with luminosty L, effective temperature T_{eff}, mass M, age τ', and composition Z. For any star along an isochrone, the relations connecting luminosity, effective temperature, and age are derived from the library of stellar models, while the flux $f_\lambda(M, \tau', Z)$ emitted by such a star is obtained from the library of stellar spectra. Sources of stellar tracks, isochrones, spectra, and SSPs in different photometric systems are taken from Bertelli et al. (2008, 2009).

Cosmological evolution of magnitudes and colors. In the course of this study, we need the magnitudes and colors of the galaxies not only in the rest-frame, but also as a function of the redshift. Following Guiderdoni & Rocca-Volmerange (1987), the apparent magnitude of a galaxy at redshift z in a passband $\Delta\lambda$ is

$$m(z) = (m - M)_{\rm bol}(z) + K(z) + E(z) + M(0, t_0), \tag{31}$$

where $K(z)$ and $E(z)$ are the cosmological and evolutionary corrections

$$K(z) = M(z, t_0) - M(0, t_0) \tag{32}$$

$$E(z) = M(z, t_z) - M(z, t_0) \tag{33}$$

and where $M(0, t_0)$ is the absolute magnitude in the passband $\Delta\lambda$ derived from the rest-frame spectrum of the galaxy at the current time, $M(z, t_0)$ is the absolute magnitude in the passband $\Delta\lambda$ derived from the spectrum of the galaxy at the current time, but redshifted at z, and $M(z, t_z)$ is the absolute magnitude in the passband $\Delta\lambda$ obtained from the spectrum of the galaxy at the time t_z and redshifted at z.

7. The Cosmic Star Formation Rate from Theory

It is worth emphasizing from the very beginning that in the course of the analysis and companion discussion, we use two

mass scales: (i) the scale of the halo masses, i.e., we refer to galaxies by their halo mass, which is roughly coincident with the total mass ($M_G \equiv M_{\rm DM} + M_{\rm BM} \simeq M_{\rm DM}$) to determine the number of halos per unit volume as a function of the halo mass and redshift. (ii) The scale of the baryonic component hosted by a halo, consisting of gas and stars. This scale is used to read from the sample of chemical models their SFR and photometric properties (magnitudes and colors) as a function of the BM mass, age, redshift, etc. The relationship between the two mass scales is given in the first two columns of Table 3.

Second, we use the grids of models of the group B, choosing the one appropriate to the mass halo, according to the mass scale $M_{\rm BM} \simeq M_{\rm DM}/6$. We have already described these models in the previous section. However, we recall here that for each model, we know both the SFR and the SSFR, the abundance of metals $Z(t)$ (for the present aims, the total metallicity is fully adequate), the mass in gas $M_g(t)$ and the mass in stars $M_s(t)$, the integrated magnitudes in the passbands $M_{\Delta\lambda}$ of the Johnson-Cousins and/or *HST*-WFPC photometric systems, the cosmological evolution of these magnitudes, i.e., the $K_{\Delta\lambda}$ and $E_{\Delta\lambda}$ corrections as a function of the redshift.

It is worth recalling here that these models not only fit the main average properties of the galaxies in the local and distant Universe, see for instance Bressan et al. (1994), Tantalo et al. (1998), and Tantalo et al. (2010), but also their SFHs agree with the results from NB-TSPH simulations of galaxy formation in cosmological context and according to the so-called early hierarchical scheme (Chiosi & Carraro 2002; Merlin & Chiosi 2006, 2007; Merlin et al. 2012). Therefore, the simple infall models presented here can be safely used to study the mean properties of galaxies in the context of the early hierarchical view of galaxy formation and evolution.

7.1. Distribution of Halos in Number and Mass

We start the analysis by looking at the mass distribution of the DM halos at each value of the redshift. This is simply derived as the number of DM halos within a small interval Δz centered on few selected values of the redshift ($\Delta z = 0.02$). The results are listed in Table 2 and are plotted in Figure 7. The visual inspection of Figure 2 yields a qualitative estimate of the maximum value of the mass distribution at each redshift, which means that DM halos with mass in excess of this value have such a low probability of occurrence that they can be neglected for any practical purpose. The histograms of Figure 7 shows the comoving number density of halos as a function of the halo mass for three selected values of the redshift, namely $z = 20$ (short dashed line), $z = 6$ (long dashed line), and $z = 0$ (solid line). The mass distribution for all other values of redshift can be easily derived from the entries of Table 2. It is worth calling the attention on the steeper decrease in the number of halos at increasing halo mass and increasing redshift. While for $z = 0$ each step of the histogram roughly decreases by the same amount, this is not the case for $z = 6$ and higher, in which the steps decrease more and more at increasing halo mass. This behavior of the number frequency distribution has far-reaching consequences.

7.2. The Reference Case for the SFRD(z)

In Figure 8 we present three groups of data:

(i) The integrated absolute U magnitude of the model galaxies as a function of redshift (on a logarithmic scale); each galaxy is indicated with a different color code. As expected, the absolute magnitude first decreases (the luminosity increases) and then increases (the luminosity decreases) as the redshift decreases toward zero. The peak in the luminosity occurs when the rate of star formation is maximum.

(ii) The total luminosity and total magnitude in the U passbands of all the galaxies present in the ideal sample contained in 1 Mpc^3 according to the Lukić et al. (2007) statistics. The total U flux is given by

$$[F_{\Delta\lambda}(z_j)]_T = \sum_i N_i(M_{\rm DM}, z_j) F_{\Delta\lambda,i} \Delta z_j, \quad (34)$$

where $[F_{\Delta\lambda,i}]_T$ is the flux in the chosen passband of the generic galaxy i of mass $M_{G,i} = M_{{\rm BM},i} + M_{{\rm DM},i}$, and Δz_j is the generic redshift range centered on z_j and defined by $0.5 \times [z_j - z_{j-1}]$ and $0.5 \times [z_{j+1} - z_j]$. The number of galaxies $N_i(M_{{\rm DM},i}, z_j)$ at the generic redshift z_j is calculated using the mass scale of the DM halos, whereas the photometric properties are obtained using the mass scale of BM and more precisely, the mass in stars existing in the galaxy at the time t or redshift z. The indices i and j run over the whole grids of masses and redshifts under considerations. The total U magnitude is shown by the dotted blue line in Figure 8. The magnitude scale along the y-axis is on the left-hand side of the figure.

(iii) A similar procedure is applied to derive the total true SFR for the galaxies in the same ideal sample contained in a volume of 1 Mpc^3,

$$[{\rm SFRD}(z_j)]_T = \sum_i N_i(M_{\rm DM}, z_j) {\rm SFR}_i(z_j) \Delta z_j, \quad (35)$$

where the indices i and j run over the whole mass and redshifts grids as before. The SFRD(z) is the red solid curve. The scale for the SFR is along the y-axis at the right-hand side of the figure. The SFRD(z) has the same trend as the total U magnitude, thus confirming that the UV light is a good tracer of star formation.

The results are shown in Figure 9 and compared with the data and the empirical best-fit relation of Madau & Dickinson (2014) given by Equation (1; dotted black line).

Theory and data almost agree in the location of the peak (redshift $z \simeq 2$) and at the low-redshift side (descending branch), whereas they may differ by up to a factor of three beyond the peak toward the past. The provisional conclusion we could derive at this stage is that the theoretical SFRD(z) and the data of Madau & Dickinson (2014) agree with each other fairly well, thus indicating that our simple model of the cosmic SFR reproduces the observational data well.

It is worth emphasizing here that for each bin of redshift, the SFRD(z) is obtained by summing the contribution from galaxies of different mass, and in particular, different history and stage of star formation. For instance, in the redshift interval $1 < z < 3$, we may have both galaxies with increasing SFR and galaxies with descending SFR. The change in the slope of the SFRD(z) at $z \simeq 2$ implies a change in the slope of the mean SFR in the galaxy population. At $z > 2$ galaxies with increasing SFR dominate, while the opposite holds at $z < 2$, where they balance each other at $z \simeq 2$. The SFRD(z) does not indicate the behavior of individual galaxies, but only the current mean behavior of whole galaxy population (see also the discussion in Section 7.3 below).

Table 2
Expected Number Densities of DM Halos per $[Mpc\ h^{-1}]^3$ at Varying the DM Mass and Redshift z

z	10^7	10^8	10^9	10^{10}	10^{11}	10^{12}	10^{13}
20.00	0.113E+01	0.159E–01	0.482E–04	0.857E–08	0.346E–14	0.506E–24	0.000E+00
15.00	0.658E+01	0.215E+00	0.390E–02	0.111E–04	0.930E–09	0.335E–16	0.120E–45
10.00	0.240E+02	0.152E+01	0.753E–01	0.180E–02	0.762E–05	0.566E–09	0.176E–18
8.00	0.347E+02	0.274E+01	0.168E+00	0.756E–02	0.104E–03	0.103E–06	0.691E–13
6.00	0.433E+02	0.415E+01	0.293E+00	0.219E–01	0.778E–03	0.601E–05	0.568E–09
4.00	0.433E+02	0.485E+01	0.389E+00	0.419E–01	0.304E–02	0.994E–04	0.312E–06
2.00	0.319E+02	0.395E+01	0.376E+00	0.507E–01	0.585E–02	0.437E–03	0.190E–04
1.00	0.235E+02	0.299E+01	0.322E+00	0.461E–01	0.610E–02	0.554E–03	0.638E–04
0.80	0.218E+02	0.278E+01	0.309E+00	0.445E–01	0.601E–02	0.559E–03	0.755E–04
0.60	0.202E+02	0.257E+01	0.295E+00	0.427E–01	0.586E–02	0.556E–03	0.869E–04
0.40	0.185E+02	0.237E+01	0.280E+00	0.408E–01	0.568E–02	0.546E–03	0.973E–04
0.20	0.169E+02	0.217E+01	0.266E+00	0.387E–01	0.545E–02	0.529E–03	0.106E–03
0.00	0.157E+02	0.201E+01	0.254E+00	0.371E–01	0.525E–02	0.512E–03	0.111E–03

Note. The DM masses are in $M_\odot\, h^{-1}$.

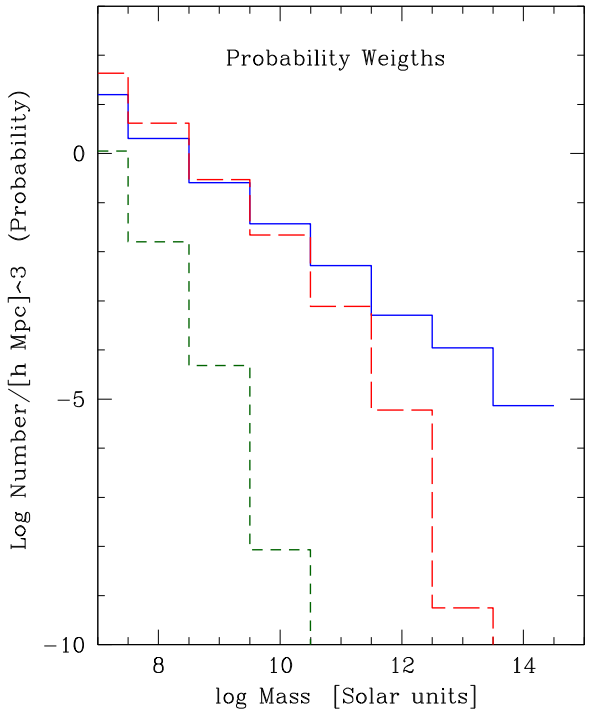

Figure 7. Expected number of DM halos as a function of the halo mass $M_{\rm DM}$ at three selected values of the redshift, namely $z = 20$ (short dashed line in dark green), $z = 6$ (long dashed line in red), and $z = 0$ (solid blue line).

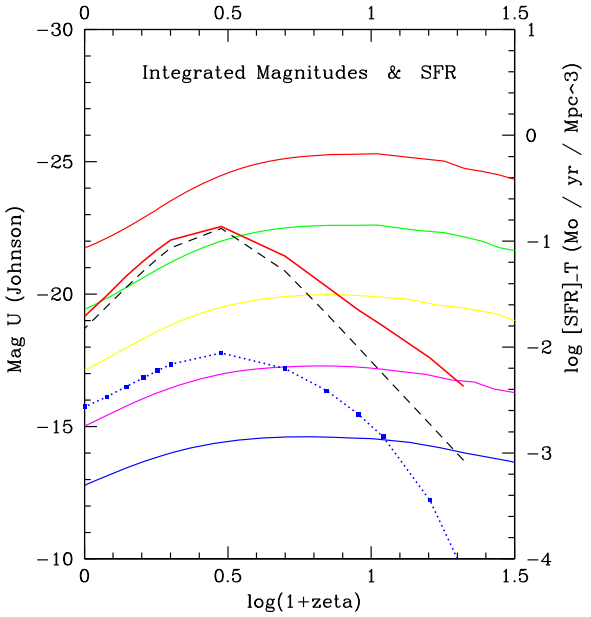

Figure 8. Three groups of data are displayed: (i) the integrated absolute U magnitude of the model galaxies as a function of the redshift (on a logarithmic scale); each galaxy is indicated by a solid line with a different color code according to the mass of the BM component. The galaxies on display have BM masses of 10^8 to $10^{12}\ M_\odot$ from bottom to top (blue, magenta, yellow, green, and red). (ii) The total magnitude in the U passbands of all the galaxies present in the ideal sample of 1 Mpc^3 volume according to the Lukić et al. (2007) statistics (the blue dotted line with filled circles). The y-axis for the magnitudes is at the left-hand side of the panel. (iii) The SFRD(z) for the same sample of galaxies (the red solid line). Finally, the analytical fit of the Madau & Dickinson (2014) SFRD (the black dashed line). The y-axis for the SFRD is at the right-hand side of the figure.

It is also interesting to see the contribution to the SFRD by galaxies of different mass at different redshifts. This is displayed in Figure 10, where we show the product $\mathrm{SFR}(z, M_G) \times N(z, M_G)$ as a function of the total galaxy mass M_G and redshift. Each line is at constant redshifts. The color code bins the lines into three groups of redshift (red lines for redshifts $z = 20$, 15, 10, 8 and 6; green lines for $z = 4$, 2, 1, 0.8 and 0.6; orange lines for $z = 0.4$ and 0.2; and finally, the blue dashed line is for $z = 0$). At high redshifts, the dominant contribution is from the low-mass galaxies, it shifts to the contribution from higher mass galaxies at intermediate redshifts, and gradually returns to the low-mass range for redshifts tending to zero. Looking at the case $z = 0$ in the $[\mathrm{SFR}(M_G) \times N(M_G)]$ versus M_G plane (Figure 10), the slope $d\log[\mathrm{SFR}(M_G) \times N(M_G)]/d\log M_G \simeq -0.3$ for M_G passes from 10^8 to $10^{12}\ M_\odot$, i.e., it mildly decreases with the galaxy mass.

To strengthen the above conclusion, we examine the correlations of the SFR and SFRD(z) with the star mass M_s and/or $M_{\rm BM}$ as a function of the redshift. Thanks to the high efficiency of star formation (ν) in all the models, $M_s \simeq 0.97\, M_{\rm BM}$. The relationships in question are shown in the two panels of Figure 11. The top panel shows the SFR versus M_s at different redshifts, while the bottom panel displays the SFRD(z) at $z = 0$. The slope and zero point of the SFR versus M_s relationships change with the redshift. The slope

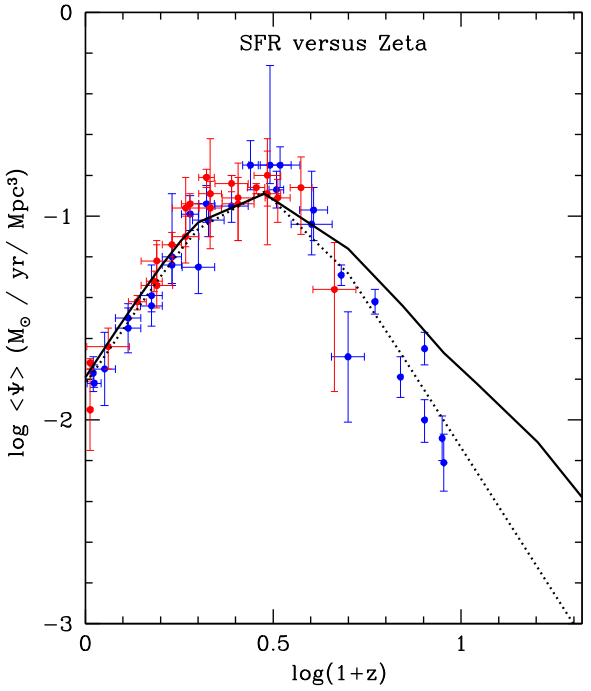

Figure 9. Theoretical SFRD(z) predicted from galaxy models of group B (solid black line) compared with the observational data (blue and red filled circles with error bars) and the analytical fit of Madau & Dickinson (2014; dotted line).

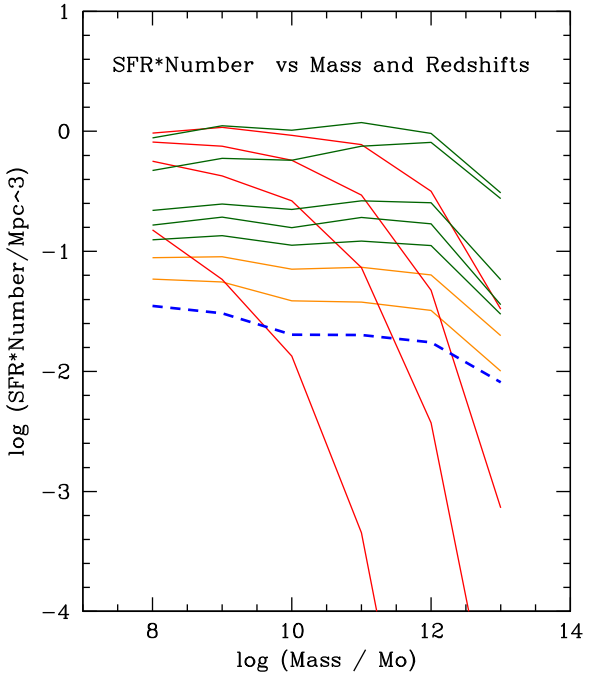

Figure 10. Contribution to the SFRD(z) from galaxies of different mass at varying redshifts. The red lines show redshifts $z = 20$, 15, 10, 8, and 6; the green lines show $z = 4$, 2, 1, 0.8, and 0.6; the orange lines show $z = 0.4$ and 0.2, and finally, the blue dashed line shows $z = 0$.

decreases at decreasing redshift: specifically, at $z = 15$ indicated by the blue line, $z = 1.0$ and $z = 0.6$ (the green and orange lines, respectively), and at $z = 0$ (the dark red line). These theoretical relationships are compared with the observational relationship by Renzini & Peng (2015), which is shown with the red solid line labeled RP15. The theoretical relation at

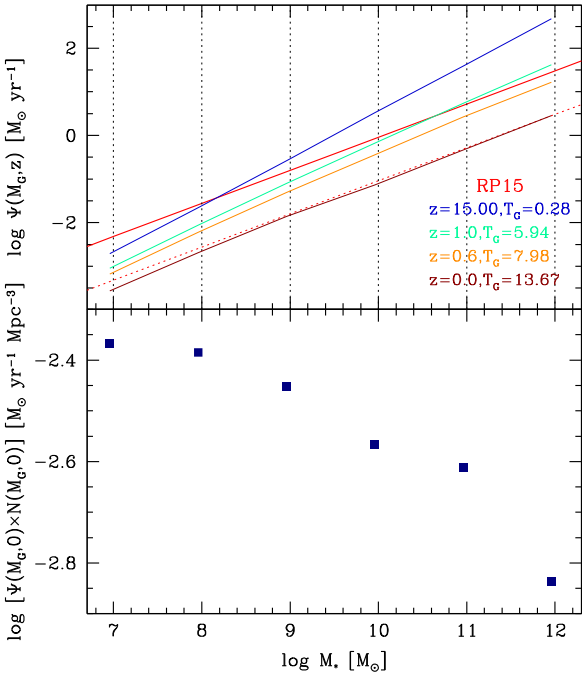

Figure 11. Top panel: SFR vs. the galaxy stellar mass M_s at different epochs in galaxies of different BM mass. Since these models are without galactic winds, $M_s \simeq 0.97 \times M_{\rm BM}$. The blue solid line shows $z = 15$, the green line shows $z = 1.0$, the orange line shows $z = 0.6$, and finally, the dark red line shows $z = 0$. The solid red line labeled RP15 plots the observational data from Renzini & Peng (2015) for active galaxies. Finally, the red dotted line is the RP15 lin decreased by factor of 10 (see the text for details). Bottom panel: product SFR(0) $\times$ $N(M_G, 0)$ vs. mass in stars M_s of each galaxy in comoving Mpc^3.

$z = 0$ has the same slope as that by Renzini & Peng (2015) and differs in the zero point. It coincides with the RP15 lowered by a factor of 10 (red dotted line). Model galaxies at $z = 0$ have a minimum value of star formation, therefore they belong to either the group called "green valley" galaxies or possibly even to the group of quiescent objects. They could rise to the values of Renzini & Peng (2015) by allowing the formation redshifts to span a wider range of values. The key result of this panel is that the slope of the SFR versus M_s relation is the same as that of the observational data over a wide range of redshifts ($0 \leqslant z < 1$). In the bottom panel the product SFR $\times$ $N(M_G, 0)$ decreases at increasing star mass of the galaxies. Furthermore, there may be a qualitative agreement with the data of Figure 8 of Speagle et al. (2014; their Figure 8), who find that the main-sequence slope of the star-forming galaxies increases with redshift, i.e., the conversion of gas into stars decreases with time for all masses, the massive stars in particular. This feature, otherwise known as "downsizing" from the observational point of view, appears after a mere application of the $N(M_G, z)$, thus it perfectly agrees with concordance Λ-CDM cosmogony. Finally, there is a point to note in the bottom panel: at a first sight, the case with $M_s = 10^{11}\,M_\odot$ seems to deviate from the expected trend due to its apparently higher value. To single out the cause of this is a cumbersome affair. It is most likely due to an inaccuracy in the derivation of the galaxy number densities for galaxy masses in the high-mass end of the distribution. Although it is not in plain contrast with other values of stellar mass, we plan to highlight the issue by investigating other halo mass functions in the literature (see Murray et al. 2013, and references)

Table 3
Parameters Adopted in the Chemical Models

M_{BM}	M_{DM}	R_{BM}	R_{DM}	ζ	τ	ν	τ/ν	τ	ν	τ/ν	τ	ν	τ/ν
						Group A			Group B			Group C	
10^7	6×10^7	0.13	1.35	0.3	0.01	10.0	0.003	6.0	10.0	0.6	10.0	0.1	100
											10.0	1.0	10
											10.0	10.0	1
10^8	6×10^8	0.28	2.90	0.3	0.01	10.0	0.003	5.0	10.0	0.5	8.0	0.1	80
											8.0	1.0	8
											8.0	10.0	0.8
10^9	6×10^9	0.61	6.26	0.3	0.01	10.0	0.003	4.0	10.0	0.4	6.0	0.1	60
											6.0	1.0	6
											6.0	10.0	0.6
10^{10}	6×10^{10}	1.32	13.48	0.3	0.01	10.0	0.003	3.0	10.0	0.3	4.0	0.1	40
											4.0	1.0	4
											4.0	10.0	0.4
10^{11}	6×10^{11}	2.85	29.04	0.3	0.01	10.0	0.003	2.5	10.0	0.2	3.0	0.1	30
											3.0	1.0	3
											3.0	10.0	0.3
10^{12}	6×10^{12}	6.13	62.53	0.3	0.01	10.0	0.003	2.0	10.0	0.2	2.0	0.1	20
											2.0	1.0	2
											2.0	10.0	0.2

Note. Masses are in $M_\odot$, the timescale τ is in Gyr, and the radii R_{BM} and R_{DM} are in kpc.

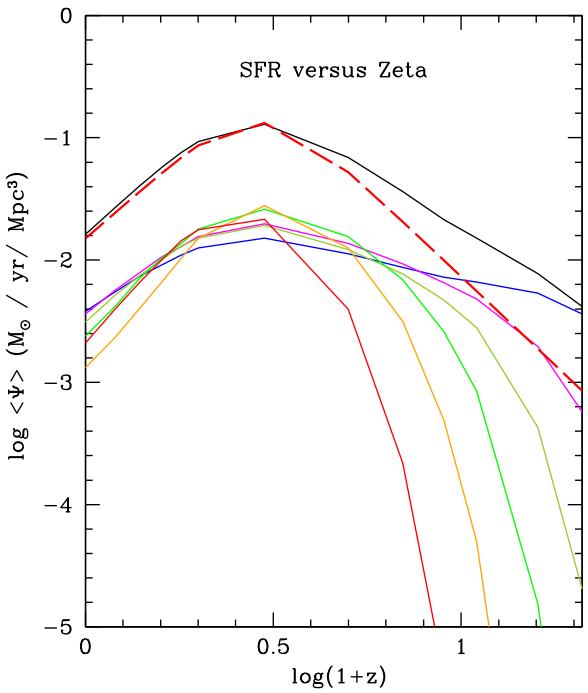

Figure 12. Contribution to the total SFRD(z) of Figure 9 from galaxies of different mass. The top solid line is the theoretical SFRD(z), while the dashed line is the analytical fit of the data by Madau & Dickinson (2014). Finally, the remaining lines are the partial contributions the the SFRD(z) by galaxies of different BM mass from $10^{12}\,M_\odot$ (bottom) to $10^7\,M_\odot$ (top).

We conclude this section with the provisional result that our simplified model for the evolution of the SFRD(z) nicely agrees with the observational data. However, it would be of general interest to single out the physical ingredients that are ultimately responsible ofor this result. This is the subject of a few ad hoc designed experiments that are briefly illustrated in the following sections.

7.3. Dissecting the SFRD(z)

The first test to perform is to dissect the total SFRD(z) in its components, i.e., to single out the functions SFR$D(z)_{M_G}$ whose sum at each z yields back the total SFRD(z). These are shown in Figure 12. Remarkably, all functions peak at $z \simeq 2$. The decrease in partial SFRDs at either side of the peaks cannot be attributed to number density alone (see the curves in the Lukić et al. (2007) and our Figure 2) because either they are still increasing toward their peak value (case of the high-mass galaxies), or they have already reached their peak at higher redshifts ($z \simeq 5$), as in the case of the low-mass galaxies (this mirrors the combined effects of the gravitational collapse and their destruction in the hierarchical aggregation). The only plausible explanation is that the SFRD(z) peak mirrors the superposition of the SFR[$(t(z)$] s in existing galaxies, which reach the peak in their star-forming activity at roughly the same time. In more detail, in the past ($z > 5$–6), the dominant contribution came from low-mass objects; around the peak interval, all galaxies contribute by nearly equal amounts, even though those with masses in the range 10^{10} to $10^{11}\,M_\odot$ are more important; finally, the low-mass galaxies again dominate the contribution at low redshifts ($z < 1$–2).

7.4. Changing the Ratio M_{DM} to M_{BM}

It is worth examining the effect of adopting a different ratio $\beta = M_{DM}/M_{BM}$. Of the various possibilities, one is particularly interesting, i.e., $\beta = 1$: DM and BM are present in equal amounts. The effect of this assumption on the first and second building blocks (the number of DM halos of a given mass as a function of the redshift, and the galaxy chemical models) are easy to predict. The $N(M_{DM}, z)$ distribution remains the same,

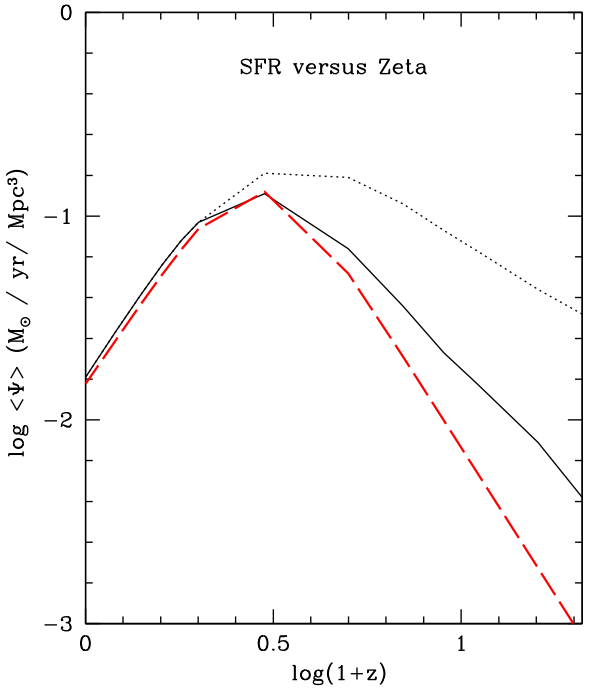

Figure 13. Changing the relation $M_{\rm BM} = \beta^{-1} M_{\rm DM}$. The black dotted line shows the SFRD(z) derived from the arbitrary assumption that $\beta = 1$, equal amounts of DM and BM per galaxy. The red dashed line shows the analytical best fit of the observational data of Madau & Dickinson (2014) and the solid black line the theoretical SFRD(z) of Figure 9, obviously obtained with $\beta = 6$.

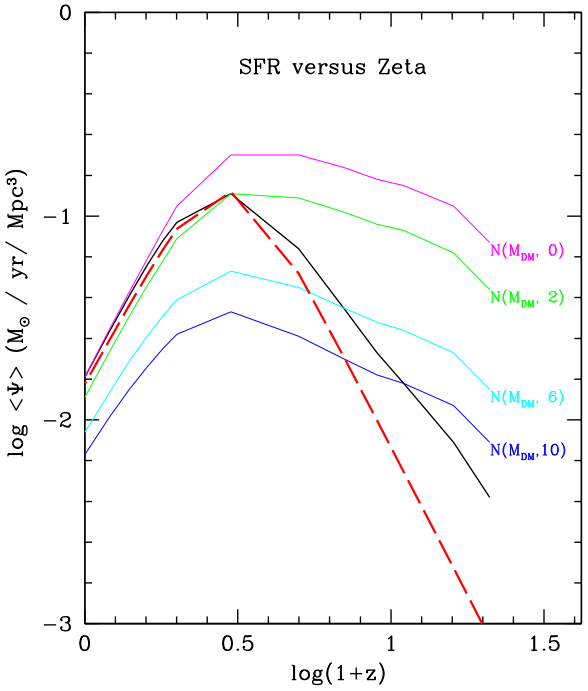

Figure 14. Changing the $N(M_{\rm DM}, z)$ relationship. See the text for details.

and no particular remark has to be made. The chemical models describing the evolution of the BM component within the DM halos remain unchanged at least in our simplified picture, in which the dynamical interaction of DM and BM is neglected. Some effect would occur on the onset of galactic winds (if present) because the gravitational potential of the gas depends on the ratios $M_{\rm BM}/M_{\rm DM}$ and $R_{\rm BM}/R_{\rm DM}$; the effect is small, however, and does not exceed a factor of a few percent. The main difference caused by the new relationship between BM and DM becomes visible when we calculate $[\mathrm{SFRD(z)}]_T = \sum_i N(M_{\rm DM}, z)\mathrm{SFR}_i(M_{\rm DM}, z)\Delta z$ because the $\mathrm{SFR}_i(M_{\rm DM}, z)$ that was the SFR of the BM galaxy with mass $M_{\rm BM} = M_{\rm DM}/\beta$ now is the SFR of the BM galaxy with $M_{\rm BM} = M_{\rm DM}$: there can be a large factor in between that depends on the redshift. In other words, at a given total mass M_G, there is more BM to consider, so the SFR is higher at early epochs. The new cosmic SFRD(z) and the comparison of it with the reference one and the observational SFRD(z) of Madau & Dickinson (2014) is shown in Figure 13. The new SFRD(z) much resembles one of the reference case, nearly coincides with it on the tail from $z = 1$ to $z = 0$, but after that, it flattens out and runs well above the reference case (it peaks at about $z = 3$ instead of $z = 1$ to $z = 2$ and runs above it by a factor of about three at higher redshifts). One is tempted to argue that the cosmic SFRD(z) could be a good tracer of the amount of DM with respect to BM.

7.5. Changing the $N(M_{\rm DM}, z)$ Relationship

At each redshift, the gravitational aggregation of lumps of DM and BM in objects of increasingly higher total mass is described by the function $N(M_{\rm DM+BM}, z)$, whose mass dependence is customarily approximated to $N(M_{\rm DM}, z)$ thanks to the high ratio $M_{\rm DM}/M_{\rm BM}$. However, the exact shape of the function $N(M_{\rm DM}, z)$ is still uncertain, even if the function we have adopted may be a good approximation of the real one. Based on these considerations, it comes naturally to pose the question how the cosmic SFRD(z) would change if the underlying mass function of DM halos were different from the function that is currently in use. To answer the question

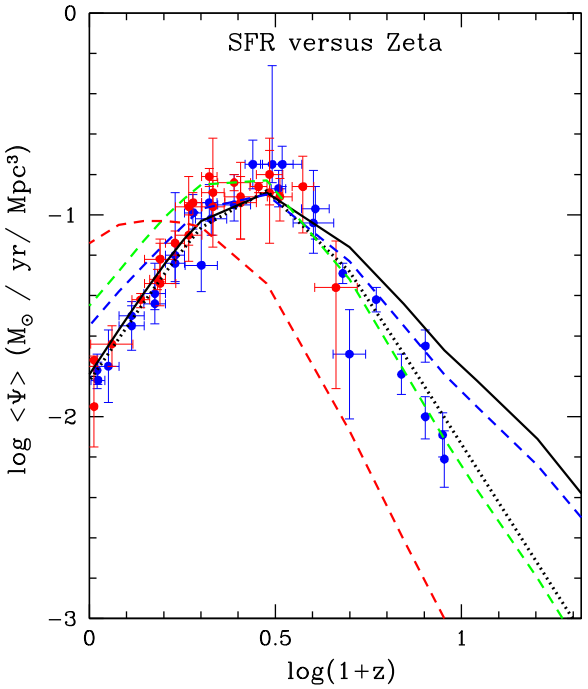

Figure 15. Effect of the intrinsic efficiency ν on the SFRD(z) derived from models of groups C (dashed lines) and B (solid line) and the comparison with observational data (filled circles with error bars) and their analytical fit (dotted line) of Madau & Dickinson (2014). The three lines for the models of group C refer to the different ν under consideration (0.1, 1, and 10 from the bottom to the top of the figure).

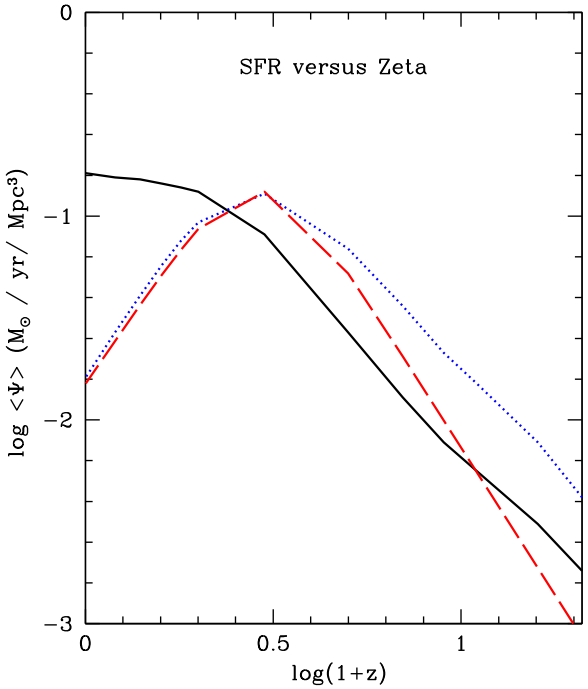

Figure 16. Cosmic SFRD(z) predicted by galaxy models whose rate of star formation is constant with time and equal to the mean value expected for models of group B (black solid line). The mean SFR is different for each galaxy. The value is calculated as $M_s(T_G) = T_G^{-1} \int \psi(t) dt = \langle \Psi(t) \rangle T_G$, where $M_s(T_G)$ is the present-day mass in stars of the galaxy with the same total mass, but normal-time-varying $\Psi(t)$, and T_G is the present-day age of the galaxy. The blue dotted line shows the SFRD(z) for models of group B, and the red dashed line shows the observational fit by Madau & Dickinson (2014).

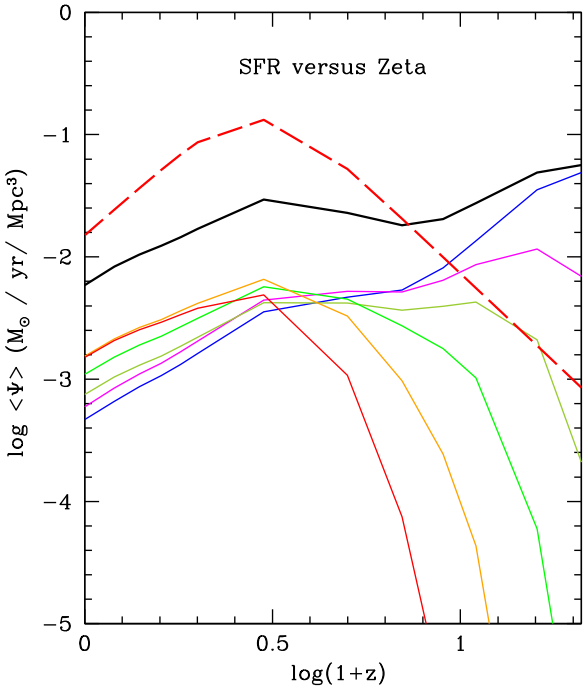

Figure 17. Predicted SFRD(z) for the closed-like models of type A (see the text for details). The thin lines show the partial contribution to the SFRD(z) from galaxies of different mass: from top to bottom, the galaxies are labeled according to their BM mass scale from 10^7 to $10^{12}\,M_\odot$. The broad solid line shows the total SFRD(z). Finally, the dashed line shows the analytical fit of the data by Madau & Dickinson (2014).

without venturing into arbitrary speculations, we perform a simple numerical experiment. We assume that the mass distribution does not vary with redshift, but only with mass, and test four mass distributions: namely $N(M_{\rm DM}, 0)$, $N(M_{\rm DM}, 2)$, $N(M_{\rm DM}, 6)$, and $N(M_{\rm DM}, 10)$. This means that while the rate of star formation in the model galaxies varies with the redshift, their number does not. With this recipe, we calculate the corresponding SFRD(z). We refer to this as the *false SFRDs*. The results are shown in Figure 14. No renormalization was applied to the false SFRD(z) to cause their peak value to coincide with the observational value reported by Madau & Dickinson (2014). It is interesting to note that the false SFRDs resemble the real one at low redshift ($z \leqslant 2$), strongly deviate from it at intermediate redshifts, and eventually again approach it at high redshifts. Since the SFRs of the model galaxies are the same as those of the reference frame, this clearly shows that $N(M_{\rm DM}, z)$ is the term that mainly drives the shape of the cosmic SFRD(z). The gravitational building-up of galaxies at early epochs ($z \geqslant 1$–2) yields the rising branch, while in more recent epochs ($z \leqslant 1$–2), the declining of the mean SFR in galaxies by gas consumption most likely prevails.

7.6. Changing the Efficiency of Star Formation ν

The rate of star formation we have adopted also contains the efficiency parameter ν, whose effects are worth investigating. Figure 15 shows the SFRD(z) expected for models of type C in which the efficiency parameter ν of the SFR is decreased from $\nu = 10$ (top long dashed line) to $\nu = 1$ (middle long dashed line) and even to $\nu = 0.1$ (bottom long dashed line). Together with the observational data (filled circles), we plot the analytical fit (dotted line) by Madau & Dickinson (2014), and finally, the theoretical SFRD(z) for models B (the solid black line). It is soon evident that models with an SFR that is too low ($\nu = 0.1$) can be ruled out because they deviate too far compared with the observational data. The agreement between theory and observational data is good for case B ($\nu = 10$) and also case C models with a high efficiency of SFR $\nu = 1$ and $\nu = 10$, both cases are somewhat higher than observed on the descending branch toward $z = 0$, however.

7.7. Changing the SFH of Galaxies

It has repeatedly been said that an important requisite to obtain the observed SFRD(z) is that the star formation in galaxies starts very low, increases to a peak value, and then declines because of gas consumption. How legitimate is the kind of temporal dependence of the SFR we have been using so far? In other words, can we obtain the same SFRD(z) using different types of SFR?

To test this point, we explore here two different alternatives: (i) in each galaxy, the rate of star formation is constant and equal to a suitable value so that the desired amount of stars is obtained; and (ii) the rate of star formation is a mere exponentially decreasing function from a maximum value at the beginning to the present-day value.

Constant star formation. The analysis is made by means of models B, for which we calculate the mean SFR as

$$\langle \mathrm{SFR} \rangle = \frac{\int_0^{T_G} \Psi(t) dt}{T_G} \Rightarrow M_s(T_G) = \langle \mathrm{SFR} \rangle \times T_G, \qquad (36)$$

Table 4
Characteristic Quantities of the Models of Group B at the Onset of the Galactic Wind

Standard Galactic Winds and SFR										
M_{BM}	τ	ν	t_{GW}	$G_{g,GW}$	$G_{s,GW}$	Z_{GW}	$\langle Z_{GW}\rangle$	SFR_{GW}	$\lvert\Omega_{g,GW}\rvert$	$E_{th,GW}$
1.0×10^{7}	6	10	0.007	0.010	0.001	0.0001	0.0001	1.05E-03	1.72E-02	9.13E+00
1.0×10^{8}	5	10	0.007	0.011	0.001	0.0001	0.0001	1.06E-02	1.75E+00	9.27E+01
1.0×10^{9}	4	10	0.010	0.011	0.001	0.0001	0.0001	1.09E-01	1.80E+02	9.15E+02
1.0×10^{10}	3	10	0.010	0.012	0.001	0.0008	0.0008	1.21E+00	2.01E+04	2.13E+04
1.0×10^{11}	2	10	0.100	0.030	0.019	0.0135	0.0083	2.95E+01	5.22E+06	5.24E+06
1.0×10^{12}	2	10	1.010	0.040	0.362	0.0385	0.0311	4.03E+02	5.17E+08	5.32E+08
Modified SFR and Conditions for the Onset of Galactic Winds										
M_{BM}	τ	ν	η_{th}	$G_{g,GW}$	$G_{s,GW}$	Z_{GW}	$\langle Z_{GW}\rangle$	SFR_{GW}	$\Omega_{g,GW}$	$E_{th,GW}$
1.0×10^{7}	6	10	0.00001	0.033	0.920	0.0440	0.0357	2.89E-04	1.87E-01	1.58E-01
1.0×10^{8}	5	10	0.00010	0.020	0.928	0.0445	0.0365	2.14E-03	1.12E+01	9.07E+00
1.0×10^{9}	4	10	0.00500	0.040	0.903	0.0488	0.0348	1.58E-02	2.24E+03	2.07E+03
1.0×10^{10}	3	10	0.01000	0.007	0.928	0.0485	0.0371	6.14E-02	3.99E+04	3.39E+04
1.0×10^{11}	2	10	0.10000	0.007	0.923	0.0514	0.0370	3.42E-01	2.79E+06	2.54E+06
1.0×10^{12}	2	10	0.30000	0.008	0.913	0.0556	0.0366	1.51E+00	9.24E+07	8.45E+07

Note. The following quantities are shown: the baryonic mass M_{BM} in solar units, the accretion timescale τ in Gyr, the efficiency of star formation ν, the time t_{GW} in Gyr of the occurrence of the stellar wind, the gas fraction $G_{g,GW}$, star mass fraction $G_{s,GW}$, the current metallicity Z_{GW}, the mean metallicity $\langle Z_{GW}\rangle$, the SFR SFR_{GW}, the gas gravitational potential energy $\omega_{g,GW}$, and the gas thermal energy $e_{th,GW}$ at the onset of the galactic wind (both are per unit mass of the galaxy and in erg g^{-1}). The top models refer to the case of a standard rate of star formation and condition for galactic wind. The bottom models refer to a case in which the thermal budget given to the interstellar medium is artificially cooled down to a suitable value, and at the same time, the SFR is lowered by means of ν_{eff} so that the galactic wind can only occur at the present time. See the text for details.

where T_G is the galaxy age, $\Psi(t)$ the current SFR, and $M_s(T_G)$ the total mass in stars at the galaxy age T_G. All these quantities are known from the previous calculation of models B. Since no galactic winds are considered in models of group B and nearly all BM mass is converted into stars ($\simeq$90%), for all practical purposes, their $\langle$SFR$\rangle$ can be estimated by inserting in Equation (36) $M_s(T_G) = 0.9 \times M_{BM}$, $T_G \simeq 13.5$ Gyr, and expressing it in $M_\odot$ yr^{-1}. With the aid of these $\langle$SFR$\rangle$, we derive the new SFRD(z) with the usual procedure and compare it with the observational one. The result is shown in Figure 16. As expected, now the cosmic SFRD(z) simply increases with decreasing redshift, thus mirroring the underlying increasing mean number density of galaxies of different mass. This finding lends strong support to our previous conclusion about the time dependence of the SFR taking place in each galaxy.

Exponentially decreasing star formation rate. To shed light on this issue, we make use of the models of group A. In all these models, the timescale of mass accretion and intrinsic star formation efficiency is $\tau = 0.01$ Gyr and $\nu = 10$. These models closely mimic the closed-box approximation. With these assumptions, the SSFR of the models is essentially a simple exponential law. Consequently, the maximum star formation occurs at the beginning of the SFH and declines thereafter. The resulting SFRD(z) is shown in Figure 17, which shows the partial contribution to the SFRD(z) from galaxies of different mass (thin lines), the total SFRD(z) (broad solid line), and the observational fit. The total SFRD(z) is very high (much higher than the observational one) at high redshift, it has a lull at intermediate values, and it remains lower than the observational one at low redshifts. The reason for this awkward behavior can be accounted for by examining the partial contribution from galaxies with different mass. First of all, galaxies with $M_G > 10^{10}\,M_\odot$ at decreasing redshift first increase, reach a peak value, and then decrease again. At $z = 0$, their contribution is comparable within a factor of five. The galaxies of lower mass at low redshift contribute less than the massive ones, the opposite occurs at high redshift, and they are also responsible for the intermediate-redshift lull. Finally, this can be attributed to the time dependence of the SSFR in each galaxy, which is simply a mere exponential law, the same as for galaxy models.

The conclusion of this experiment is that a continuously decreasing SFR from an initial maximum to the present-day value cannot generate the desired SFRD(z) unless other physical effects are introduced.

7.8. Introducing Galactic Winds

All the galaxy models used so far have been calculated without the possible presence of galactic winds (i.e., condition (22) for the onset of galactic winds has not been applied). In this section, we take the energy injection by supernova explosions and stellar winds into account and apply condition (22). In this view of the whole issue of galactic winds, the above prescription implies that when condition (22) is verified, the remaining gas is assumed to escape the galaxy, and further star formation does no longer occur. The evolution of the remnant galaxy is passive, and all the gas shed by stars formed in the previous epochs either in the form of stellar wind or supernova explosions does no longer generate new stars. In addition to this, owing to the different gravitational potential well of massive galaxies with respect to the low-mass ones, the time at which the threshold energy for galactic winds is reached occurs earlier in low-mass galaxies than in the massive ones. All this is inherent to the Larson (1974) model of galactic winds, which has been superseded by more sophisticated treatment of the wind process with the aid of NB-TSPH models

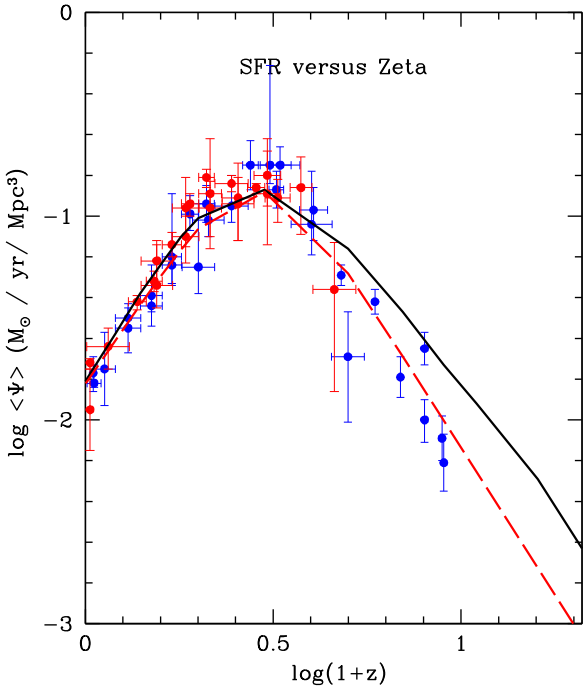

Figure 18. Predicted SFRD(z) for models of type B with galactic winds whose key data are reported in Table 4 and comparison with the observational data (filled circles) and their analytical fit (dashed line) by Madau & Dickinson (2014).

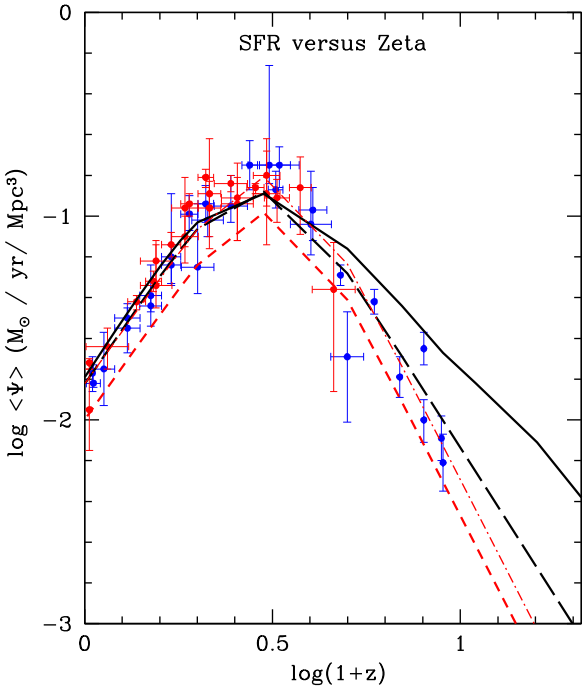

Figure 19. Theoretical SFRD(z) from models of group B (solid black line) compared with observational data (blue and red filled circles with error bars), the previous analytical fit by Madau & Dickinson (2014; long dashed line), the original empirical relationship by Madau & Fragos (2017; short dashed line), and the same shifted by the factor 0.66 to compensate for the different assumptions for the stellar IMF (dashed dotted line). See the text for details.

of galaxy formation and evolution (Chiosi & Carraro 2002; Merlin & Chiosi 2006, 2007; Merlin et al. 2012). To illustrate the point, we show in the top part of Table 4 a few key quantities for models of Group B evolved in presence of galactic winds according to the straight prescription of Larson (1974). With this prescription, galactic winds occur very early, so that the stellar content of a galaxy is hardly made. The problem can be partly cured either by decreasing the efficiency of star formation (lower values of ν) or by invoking a lower quantity of energy that is injected by supernova explosions and stellar winds into the interstellar medium (more efficient cooling of this energy). Since in doing this, a certain degree of arbitrariness is unavoidable owing to the lack of suitable constraints on the galaxy models in use, we prefer to adopt a different strategy.

This modeling of the galactic winds is not realistic because numerical NB-TSPH simulations have indicated that galactic winds are not instantaneous, but take place on long timescales. Gas heated up by supernova explosions and stellar winds that is cooled down by radiative processes not only gradually reaches the escape velocity, but also affects the efficiency of star formation because the hot gas is continuously subtracted. All this cannot be easily incorporated in the simple galaxy model we use here. To cope with this difficulty, we modify our model as follows.

First of all, to improve the cooling algorithm we use, which is not as good as the algorithm currently adopted in NB-TSPH models, we introduce an efficiency parameter $\eta_{\rm th}$ ranging from 0 (no energy feedback) to 1 (full energy feedback) and accordingly change condition (22) to

$$\eta_{\rm th} \times E_{\rm th}(t) \geqslant |\Omega_g(t)|. \tag{37}$$

Second, we change the star formation law by redefining the parameter ν as an effective efficiency given by

$$\nu_{\rm eff} = \nu \times \frac{|\eta_{\rm th} \times E_{\rm th} - |\Omega_g||}{\eta_{\rm th} \times E_{\rm th} + \Omega_g} \tag{38}$$

where ν is the usual efficiency. By decreasing the efficiency of star formation at increasing $E_{\rm th}$, we intend to mimic the fact that hot gas is likely less prone to generate stars by gravitational collapse. As consequence, the threshold stage for the onset of galactic winds may occur much later or may even be avoided at all. Less gas is turned into stars, as if part of the gas continuously escaped from the galaxy. The net SFR decreases with obvious consequences on the SFRD(z).

New models of Group B are calculated using the efficiency parameter $\nu_{\rm eff}$, and the new condition (38) for the onset of galactic winds. The values of $\nu_{\rm eff}$ are chosen in such a way that the galactic winds occur only at the present age or later. These parameters are listed in the bottom part of Table 4. Throughout their history, these models have an SFR lower than their standard counterparts, thus mimicking the most important effect of the energy feedback of evolving stars, i.e., heating up part of the gas and subtracting it from star formation. The SFRD(z) expected from these models and the comparison with the observational one of Madau & Dickinson (2014) is shown in Figure 18. Theory and observations agree above all expectations. Although our treatment of galactic wind is very crude, we suspect that galactic wind only plays a marginal role in shaping the SFRD(z).

7.9. Changing the Analytical Best Fit

We conclude the analysis by comparing the theoretical models with a new analytical best fit of the observational data by Madau & Fragos (2017), who take recent data in the redshift interval ($4 \leqslant z \leqslant 100$) into account and also the IMF by Kroupa (2001) instead of the Salpeter (1955) IMF. Changing the IMF introduces a factor 0.66 in passing from the old to the new one. The comparison is shown in Figure 19. Correcting for this factor as appropriate, the agreement between theory and observation is still there.

7.10. Comparison with N-body Cosmological Simulations

Recent attempts to model the SFRD(z) in the framework of large-scale simulations of hierarchical galaxy formation in Λ-CDM cosmogony including both DM and BM have been made possible by the new generation of numerical codes developed by Hernquist & Springel (2003), Springel & Hernquist (2003a, 2003b), Vogelsberger et al. (2012), Barai et al. (2013), and Puchwein & Springel (2013; and references therein), in which much effort is paid to include radiative cooling and heating in presence of an UV background radiation field, star formation, and associated feedback processes. The SFRD(z) in particular has been addressed by Katsianis et al. (2017; see their Figure 7) and Pillepich et al. (2017). The key results are the comoving mean SFR and cosmic SFRD as functions of look-back time and/or redshift that are very similar to those we have used here. It is worth emphasizing that the mean SFH and SFRD(z) refer to the whole slab of the Universe under examination, and not to any galaxy in particular.

In our study we have taken a different perspective: starting from galaxies whose SFH we follow in detail, we integrated over the whole population of galaxies in the same Universe slab (whose number is derived from the hierarchical growth of structures in the Λ-CDM cosmogony), and we derived the total SFRD(z).

In other words, starting from individual objects, we reconstructed the mean SFRD(z). In this context, the results of the present study are in perfect agreement with those obtained from extensive and time-consuming cosmological simulations. The novelty of the present study is that we arrive at the same conclusions with a much simpler approach, in which all physical foundations of the cosmic SFRD can be changed and separately analyzed with almost no computational time needed.

8. General Remarks and Conclusions

Before any consideration, we point out that (a) the HGF and galaxy SFR are the starring actors of the whole problem, and (b) no specific assumption is made to force the galaxy models in use to reproduce the cosmic SFRD (the choice of their leading parameter is suggested by other independent arguments). Based on the present analysis, we may conclude the following.

(i) The shape of the SFRD(z) is primarily driven by the cosmic mass distribution of galaxies, i.e., the function $N(M_G, z)$ in place at each value of the redshift. The galaxy mass distribution function in turn partly results from the growth of primordial fluctuations to the collapse stage, and partly from the aggregation of existing objects with active or quiescent star formation into new ones of higher mass (the classical hierarchical view).

(ii) The second important ingredient is the rate of star formation that takes place in individual galaxies. Only the so-called time-delayed SFR, i.e., a rate of star formation that starts low, grows to a maximum and then declines, can yield the desired SFRD(z). In the formalism of the infall models, in which the BM component (in the form of gas) flows into the gravitational potential well of DM at a suitable rate proportional to an exponential time dependence $\dot{M}_{\rm BM} \propto \exp(-t/\tau)$ and is gradually converted into stars by the law $\dot{M}_s = \nu M_g$, giving rise to the time-delayed star formation $\dot{M}_s \propto \frac{t}{\tau}\exp(-t/\tau)$. This type of SFR is able to reproduce the SFR inferred in galaxies of different morphological type (see Sandage 1986; Thomas et al. 2005) and also the SFR resulting from detailed numerical NB-TSPH simulations of galaxies (Chiosi & Carraro 2002; Merlin et al. 2012). Constant and exponentially declining SFRs cannot yield the observed SFRD(z).

However, also the intrinsic efficiency of star formation (the parameter ν) has an important role because together with the timescale of the mass accretion, it eventually drives the temporal dependence of star formation from the star formation that peaks at early epochs (high values of ν) to the star formation that is more skewed toward the present (low values of ν), passing through the interesting case of nearly constant star formation. We plan to investigate this issue in more detail in a forthcoming study.

(iii) The best galaxy models to use are those of type B or even type C with minor adjustments with respect to those in use here, which tend to produce too high metallicites. The problem can be easily solved either by simply changing the net metal enrichment per stellar generation (the parameter ζ in Equation (15)) to lower values, or by adjusting the other model parameters τ, ν, and $\nu_{\rm eff}$. Since this issue is marginal to our discussion, we leave it to future investigations. However, the agreement shown by type B and C models imposes a strong constraint on the type of star formation taking place in galaxies. It cannot be too much diluted over the Hubble time, but instead should be peaked at early epochs.

(iv) At early and late epochs (i.e., high and low redshifts), the main contribution to the SFRD(z) comes from galaxies of relatively low mass, whereas at intermediate redshifts, the contribution from intermediate-mass galaxies may equal or even exceed that from the low-mass galaxies. Although always present at all epochs, the contribution from high-mass galaxies is always smaller than that from low- and intermediate-mass galaxies.

(v) The energy feedback to the interstellar gas is only due to supernovae and stellar winds, no AGN has been considered. Radiative cooling of the injected energy is taken into account, although in a simplified fashion. This point needs to be improved. The present galaxy models are not the best to investigate the effect of galactic winds because owing to the one-zone approximation, the onset of galactic winds at a certain time means a sudden interruption of the star formation process, whereas in real galaxies and also in numerical 3D simulations of galaxy formation and evolution, galactic winds take place locally

and over very long timescales without halting star formation in the whole system. To cope with this, we preferred to decrease the efficiency of star formation as the thermal content of the gas, although the radiative cooling tends to approach and eventually overwhelm the gravitational potential energy of the gas. In general, galactic winds, even though they improve the overall agreement of the models with observational data, are found to play a secondary role in the context of the temporal evolution of the cosmic SFRD(z).

(vi) The SFRD(z) does not represent the instantaneous SFR in individual galaxies $\Psi_G[t(z)]$, but measures the mean SFR of the galaxy population in a unit volume. Therefore, it mirrors the product $\Psi_G[t(z)] \times N[M_G(t(z)]$, where M_G is the total mass of a galaxy and $t(z)$ is the particular time-redshift relation of the cosmological model of the Universe that is adopted. Using the SFRD(z) instead of $\Psi_G[t(z)]$ to model the history of single galaxies may lead to incorrect results. The opposite is also true.

(vii) We have adopted the HGF of Lukić et al. (2007), which in turn stems from the HMF of Warren et al. (2006), because it is an easy-to-use tool for our purposes. However, owing to the well-known problem of the non-universality of the fitting function $f(\sigma)$ (Tinker et al. 2008), other models for the HMF can be found (Murray et al. 2013). We plan to investigate this issue by using different HMFs.

(viii) The present approach yields results that fully agree with those from highly sophisticated large-scale numerical simulations. Therefore it should be considered as a complementary tool for exploring different assumptions concerning basic physical processes such as the star formation law and the nature and efficiency of the energy feedback.

(ix) We plan to refine the present modeling of the SFRD(z) history by replacing the simple galaxy models with a library of 3D N-body simulations of galaxy formation and evolution and also the number density evolution of galaxies of different mass, i.e., the functions $N(M_G, z)$ with the aid of ad hoc designed Monte Carlo simulations. Finally, we will follow the photometric evolution of the galaxies to investigate the relationship between the SSFR and stellar mass content in galaxies of different mass, redshift, and color.

(x) As final conclusions, we would like to briefly answer a few important questions that could be raised, such as why the SFRD(z) is low at high and low redshift. Is the quenching of SF at $z \leqslant 2$ associated with a decreasing gas supply at late epochs? Why is star formation inefficient at early times even in the absence of feedback? Why is it possible to reproduce the data without AGN feedback? What is the meaning of the particular combinations of parameters ν and τ that are required to reproduce the data?

The time (redshift) dependence of the SFR in the model galaxies is the result of the cross-effect of two physical processes: gas accretion at a suitable rate onto the galaxy potential well, and gas consumption by star formation according to a Schmidt-like law. By controlling these two parameters, the galaxy models can be tuned to match the gross features of real galaxies all along the Hubble sequence. The key feature of these galaxy models is that independently of the galaxy mass, the SFR starts low, grows to a maximum, and then declines as function of time. However, the same SFR is strong and peaked at early epochs in massive objects (with early-type galaxies as counterparts), mild and prolonged in intermediate-mass galaxies (observational counterparts are disk galaxies), and very mild and likely stretching (perhaps in recurrent bursts of activity that were not considered here) thorughout the Hubble time (observational counterparts are irregular galaxies). As we described above, this scheme is strongly supported by the body of observational data of galaxies and the N-body simulations of same. This tuning of the galaxy models we used here has been made over the years independently of the cosmic SFRD issue. At low redshift, the "quenching" of star formation, is simply caused by the fact that individual galaxies tend to run out of fuel (gas) in the star-forming activity. At high redshift, a similar trend is recovered because galaxies are still in the gas-accumulation phase and little gas has already reached the threshold density required for star formation to occur (Krumholz 2015; it is worth recalling here that stars form in very dense environments). So at these very early epochs, the natural expectation is that the star formation activity is low but growing with time. This trend would mimic the effect of some quenching at early epochs.

Our reference SFRD(z) of Figure 9, obtained with standard energy feedback from supernovae and stellar winds, with no AGNs and no galactic winds, agrees rather well with the observational one from $z = 0$ to $z = 2$ (the reference case mirrors the picture outlined above for the natural behavior of SFR in galaxies), whiöe it tends to depart from it at increasing redshift. At redshift $z \simeq 10$, it is about a factor of 2 to 3 higher than expected. The presence of galactic winds slightly improves the agreement in the latter region (see Figure 18), and perhaps some other effects like mild quenching by AGNs might completely remove the discrepancy. Our provisional conclusion is that strong and exotic quenching of the star formation in the interval $2 \leqslant z \leqslant 8$) (see, for instance, Tescari et al. 2014; Renzini 2016, and references) is not strictly needed. The only case in which either strong quenching and/or dust obscuration or both are required is when an an exponential SFR is used. However, the resulting SFRD(z) differs from the observed one in many other details and has to be discarded. Therefore, quenching does not likely play an important role in shaping the observed SFRD(z) as compared to the combined effect of the HGF $N(M_{\rm DM}, z)$ and of the $\Psi(t)$ modulated by the gradual accumulation of gas within the total gravitational potential well and conversion of it into stars. AGNs and galactic winds are of course not excluded from this picture, but they are assumed to play a less important role than customarily claimed.

We would like to thank the anonymous referee for useful critical comments that helped us to amend and improve the first version of the paper. C. Chiosi, F. Brotto, R. De Michele, and V. Politino are deeply grateful to the Heraeus Foundation for the financial support to attend the Heraeus Summer School 2016 "Origins of Stars and Planets" (August 2016, Florence, Italy) where this study was presented for the first time. C.C. would like to thank the Physics & Astronomy Department of the Padova University for the kind hospitality and computing support.

ORCID iDs

Cesare Chiosi https://orcid.org/0000-0001-7107-8196
Mauro D'Onofrio https://orcid.org/0000-0001-6441-9044

References

Abramson, L. E., Gladders, M. D., Dressler, A., et al. 2016, ApJ, 832, 7
Alavi, A., Siana, B., Richard, J., et al. 2014, ApJ, 780, 143
Angeletti, L., & Giannone, P. 1990, A&A, 234, 53
Arimoto, N., & Yoshii, Y. 1987, A&A, 173, 23
Barai, P., Viel, M., Borgani, S., et al. 2013, MNRAS, 430, 3213
Bernardi, M., Shankar, F., Hyde, J. B., et al. 2010, MNRAS, 404, 2087
Bertelli, G., Bressan, A., Chiosi, C., Fagotto, F., & Nasi, E. 1994, A&As, 106, 275
Bertelli, G., Girardi, L., Marigo, P., & Nasi, E. 2008, A&A, 484, 815
Bertelli, G., Nasi, E., Girardi, L., & Marigo, P. 2009, A&A, 508, 355
Bertin, G., Saglia, R. P., & Stiavelli, M. 1992, ApJ, 384, 423
Bouwens, R. J., Illingworth, G. D., Oesch, P. A., et al. 2012, ApJ, 754, 83
Bower, R. G., Lucey, J. R., & Ellis, R. S. 1992, MNRAS, 254, 601
Bressan, A., Chiosi, C., & Fagotto, F. 1994, ApJS, 94, 63
Buzzoni, A. 2002, AJ, 123, 1188
Cassarà, L. P., Maccagni, D., Garilli, B., et al. 2016, A&A, 593, A9
Chabrier, G. 2015, IAUGA, 22, 2224239
Chiosi, C. 1980, A&A, 83, 206
Chiosi, C., Bressan, A., Portinari, L., & Tantalo, R. 1998, A&A, 339, 355
Chiosi, C., & Carraro, G. 2002, MNRAS, 335, 335
Cucciati, O., Tresse, L., Ilbert, O., et al. 2012, A&A, 539, A31
Dolag, K., Jubelgas, M., Springel, V., Borgani, S., & Rasia, E. 2004, ApJL, 606, L97
Fattore, M. 2009, PhD thesis, Univ. Padova
Gavazzi, G., Bonfanti, C., Sanvito, G., Boselli, A., & Scodeggio, M. 2002, ApJ, 576, 135
Gibson, B. K. 1998, ApJ, 501, 675
Gibson, B. K., & Matteucci, F. 1997, MNRAS, 291, L8
Gladders, M. D., Oemler, A., Dressler, A., et al. 2013, ApJ, 770, 64
González, V., Labbé, I., Bouwens, R. J., et al. 2011, ApJL, 735, L34
Gruppioni, C., Pozzi, F., Rodighiero, G., et al. 2013, MNRAS, 432, 23
Guiderdoni, B., & Rocca-Volmerange, B. 1987, A&A, 186, 1
Guo, Q., White, S. D. M., Boylan-Kolchin, M., et al. 2011, MNRAS, 413, 101
Hennebelle, P., & Chabrier, G. 2011, in IAU Symp. 270, Computational Star Formation, ed. J. Alves, B. Elmegreen, & V. Trimble (Cambridge: Cambridge Univ. Press), 159
Hernquist, L., & Springel, V. 2003, MNRAS, 341, 1253
Hinshaw, G., Weiland, J. L., Hill, R. S., et al. 2009, ApJS, 180, 225
Hopkins, A. M. 2004, ApJ, 615, 209
Katsianis, A., Tescari, E., Blanc, G., & Sargent, M. 2017, MNRAS, 464, 4977
Kodama, T., Bower, R. G., & Bell, E. F. 1999, MNRAS, 306, 561
Kodama, T., Bower, R. G., & Bell, E. F. 2001, Ap&SS, 276, 979
Kroupa, P. 2001, MNRAS, 322, 231
Kroupa, P., Tout, C. A., & Gilmore, G. 1993, MNRAS, 262, 545
Krumholz, M. R. 2015, arXiv:1511.03457
Larson, R. B. 1974, MNRAS, 169, 229
Larson, R. B. 1991, ASP Conf. Ser. 20, Frontiers of Stellar Evolution, ed. D. L. Lambert (San Francisco, CA: ASP), 571
Lee, K.-S., Dey, A., Reddy, N., et al. 2011, ApJ, 733, 99
Limpert, E. M., Stahel, W. A., & , M. A. 2001, BioScience, 51, 341
Lukić, Z., Heitmann, K., Habib, S., Bashinsky, S., & Ricker, P. M. 2007, ApJ, 671, 1160
Ly, C., Lee, J. C., Dale, D. A., et al. 2011, ApJ, 726, 109
Lynden-Bell, D. 1975, VA, 19, 299
Madau, P., & Dickinson, M. 2014, ARA&A, 52, 415
Madau, P., Ferguson, H. C., Dickinson, M. E., et al. 1996, MNRAS, 283, 1388
Madau, P., & Fragos, T. 2017, ApJ, 840, 39
Magnelli, B., Elbaz, D., Chary, R. R., et al. 2011, A&A, 528, A35
Maio, U., Dolag, K., Ciardi, B., & Tornatore, L. 2007, MNRAS, 379, 963
Marigo, P., Bressan, A., & Chiosi, C. 1996, A&A, 313, 545
Marigo, P., Bressan, A., & Chiosi, C. 1998, A&A, 331, 564
Matteucci, F. 1994, A&A, 288, 57
Matteucci, F. 2012, Chemical Evolution of Galaxies (Berlin: Springer)
Matteucci, F. 2016, Journal of Physics Conference Series, 703, 012004
Matteucci, F., & Greggio, L. 1986, A&A, 154, 279
Matteucci, F., & Pipino, A. 2002, ApJL, 569, L69
Matteucci, F., & Tornambé, A. 1987, A&A, 185, 51
Merlin, E., & Chiosi, C. 2006, A&A, 457, 437
Merlin, E., & Chiosi, C. 2007, A&A, 473, 733
Merlin, E., Chiosi, C., Piovan, L., et al. 2012, MNRAS, 427, 1530
Mihara, K., & Takahara, F. 1994, PASJ, 46, 447
Murray, S. G., Power, C., & Robotham, A. S. G. 2013, A&C, 3, 23
Oemler, Jr. A., Dressler, A., Gladders, M. G., et al. 2013, ApJ, 770, 63
Parsa, S., Dunlop, J. S., McLure, R. J., & Mortlock, A. 2016, MNRAS, 456, 3194
Pillepich, A., Springel, V., Nelson, D., et al. 2017, MNRAS, 473, 4077
Piovan, L., Tantalo, R., & Chiosi, C. 2006a, MNRAS, 366, 923
Piovan, L., Tantalo, R., & Chiosi, C. 2006b, MNRAS, 370, 1454
Piovan, L., Tantalo, R., & Chiosi, C. 2006c, MmSAI, 77, 873
Pipino, A., Calura, F., & Matteucci, F. 2013, MNRAS, 432, 2541
Pipino, A., & Matteucci, F. 2011, A&A, 530, A98
Planelles, S., Borgani, S., Dolag, K., et al. 2013, MNRAS, 431, 1487
Portinari, L. 1998, PhD thesis, Univ. Padova
Portinari, L., & Chiosi, C. 1999, A&A, 350, 827
Portinari, L., & Chiosi, C. 2000, A&A, 355, 929
Portinari, L., Chiosi, C., & Bressan, A. 1998, A&A, 334, 505
Press, W. H., & Schechter, P. 1974, ApJ, 187, 425
Puchwein, E., & Springel, V. 2013, MNRAS, 428, 2966
Rasera, Y., & Teyssier, R. 2006, A&A, 445, 1
Reddy, N. A., Steidel, C. C., Pettini, M., et al. 2008, ApJS, 175, 48
Renzini, A. 2006, ARA&A, 44, 141
Renzini, A. 2016, MNRAS, 460, L45
Renzini, A., & Peng, Y.-j. 2015, ApJL, 801, L29
Saglia, R. P., Bertin, G., & Stiavelli, M. 1992, ApJ, 384, 433
Saito, M. 1979a, PASJ, 31, 181
Saito, M. 1979b, PASJ, 31, 193
Salpeter, E. E. 1955, ApJ, 121, 161
Sandage, A. 1986, A&A, 161, 89
Santini, P., Fontana, A., Grazian, A., et al. 2012, A&A, 538, A33
Schenker, M. A., Robertson, B. E., Ellis, R. S., et al. 2013, ApJ, 768, 196
Schmidt, M. 1959, ApJ, 129, 243
Smit, R., Bouwens, R. J., Franx, M., et al. 2012, ApJ, 756, 14
Sobral, D., Smail, I., Best, P. N., et al. 2013, MNRAS, 428, 1128
Speagle, J. S., Steinhardt, C. L., Capak, P. L., & Silverman, J. D. 2014, ApJS, 214, 15
Springel, V. 2005, MNRAS, 364, 1105
Springel, V., Di Matteo, T., & Hernquist, L. 2005a, MNRAS, 361, 776
Springel, V., & Hernquist, L. 2003a, MNRAS, 339, 289
Springel, V., & Hernquist, L. 2003b, MNRAS, 339, 312
Springel, V., White, S. D. M., Jenkins, A., et al. 2005b, Natur, 435, 629
Talbot, Jr. R. J., & Arnett, W. D. 1971, ApJ, 170, 409
Talbot, Jr. R. J., & Arnett, W. D. 1973, ApJ, 186, 51
Tantalo, R., Chinellato, S., Merlin, E., Piovan, L., & Chiosi, C. 2010, A&A, 518, A43
Tantalo, R., Chiosi, C., Bressan, A., & Fagotto, F. 1996, A&A, 311, 361
Tantalo, R., Chiosi, C., Bressan, A., Marigo, P., & Portinari, L. 1998, A&A, 335, 823
Terlevich, A. I., Caldwell, N., & Bower, R. G. 2001, MNRAS, 326, 1547
Tescari, E., Katsianis, A., Wyithe, J. S. B., et al. 2014, MNRAS, 438, 3490
Thomas, D., Maraston, C., Bender, R., & Mendes de Oliveira, C. 2005, ApJ, 621, 673
Tinker, J., Kravtsov, A. V., Klypin, A., et al. 2008, ApJ, 688, 709
Tinsley, B. M. 1972, A&A, 20, 383
Tinsley, B. M. 1980, FCPh, 5, 287
Tornatore, L., Borgani, S., Dolag, K., & Matteucci, F. 2007, MNRAS, 382, 1050
van der Burg, R. F. J., Hildebrandt, H., & Erben, T. 2010, A&A, 523, A74
Vogelsberger, M., Sijacki, D., Kereš, D., Springel, V., & Hernquist, L. 2012, MNRAS, 425, 3024
Warren, M. S., Abazajian, K., Holz, D. E., & Teodoro, L. 2006, ApJ, 646 881
Wiersma, R. P. C., Schaye, J., & Smith, B. D. 2009a, MNRAS, 393, 99
Wiersma, R. P. C., Schaye, J., Theuns, T., Dalla Vecchia, C., & Tornatore, L. 2009b, MNRAS, 399, 574
Wilkins, S. M., Trentham, N., & Hopkins, A. M. 2008, MNRAS, 385, 687